Cell Death & Differentiation (2019) 26:2157–2178
https://doi.org/10.1038/s41418-019-0291-z

Cell Death & Differentiation

ARTICLE

MINA-1 and WAGO-4 are part of regulatory network coordinating germ cell death and RNAi in *C. elegans*

Ataman Sendoel[1] · Deni Subasic[1,2] · Luca Ducoli[1,2,3] · Martin Keller[1,2] · Erich Michel[4,11] · Ines Kohler[1] · Kapil Dev Singh[1,2,12] · Xue Zheng[1] · Anneke Brümmer[5] · Jochen Imig[3,5,13,14] · Shivendra Kishore[5] · Yibo Wu[6,7] · Alexander Kanitz[5] · Andres Kaech[8] · Nitish Mittal[5] · Ana M. Matia-González[9] · André P. Gerber[9] · Mihaela Zavolan[5] · Ruedi Aebersold[6,10] · Jonathan Hall[3] · Frédéric H.-T. Allain[4] · Michael O. Hengartner[1,10]

Received: 29 June 2018 / Revised: 23 November 2018 / Accepted: 26 November 2018 / Published online: 6 February 2019

Abstract

Post-transcriptional control of mRNAs by RNA-binding proteins (RBPs) has a prominent role in the regulation of gene expression. RBPs interact with mRNAs to control their biogenesis, splicing, transport, localization, translation, and stability. Defects in such regulation can lead to a wide range of human diseases from neurological disorders to cancer. Many RBPs are conserved between *Caenorhabditis elegans* and humans, and several are known to regulate apoptosis in the adult *C. elegans* germ line. How these RBPs control apoptosis is, however, largely unknown. Here, we identify *mina-1(C41G7.3)* in a RNA interference-based screen as a novel regulator of apoptosis, which is exclusively expressed in the adult germ line. The absence of MINA-1 causes a dramatic increase in germ cell apoptosis, a reduction in brood size, and an impaired P granules organization and structure. In vivo crosslinking immunoprecipitation experiments revealed that MINA-1 binds a set of mRNAs coding for RBPs associated with germ cell development. Additionally, a system-wide analysis of a *mina-1* deletion mutant compared with wild type, including quantitative proteome and transcriptome data, hints to a post-transcriptional regulatory RBP network driven by MINA-1 during germ cell development in *C. elegans*. In particular, we found that the germline-specific Argonaute WAGO-4 protein levels are increased in *mina-1* mutant background. Phenotypic analysis of double mutant *mina-1;wago-4* revealed that contemporary loss of MINA-1 and WAGO-4 strongly rescues the phenotypes observed in *mina-1* mutant background. To strengthen this functional interaction, we found that upregulation of WAGO-4 in *mina-1* mutant animals causes hypersensitivity to exogenous RNAi. Our comprehensive experimental approach allowed us to describe a phenocritical interaction between two RBPs controlling germ cell apoptosis and exogenous RNAi. These findings broaden our understanding of how RBPs can orchestrate different cellular events such as differentiation and death in *C. elegans*.

Introduction

In recent years, a growing number of studies revealed the importance of post-transcriptional regulation of gene expression exerted by RNA-binding proteins (RBPs) for the maintenance of gene plasticity, responsiveness to environmental cues, and proper development [1–3]. RBPs can regulate transcript splicing, transport, localization, stability, and translation so that proteins are efficiently produced at the right time, at the right place, and at the proper dose to meet the cell requirements [2]. Compromising this regulation can lead to various diseases including neurological and autoimmune disorders, muscular atrophies, and cancer [4].

The large number of RBPs in the *Caenorhabditis elegans* germ line makes this tissue an excellent model for the study

These authors contributed equally: Ataman Sendoel, Deni Subasic, Luca Ducoli, Martin Keller, Erich Michel

Edited by E. Baehrecke

Supplementary information The online version of this article (https://doi.org/10.1038/s41418-019-0291-z) contains supplementary material, which is available to authorized users.

✉ Michael O. Hengartner
michael.hengartner@imls.uzh.ch

Extended author information available on the last page of the article

of post-transcriptional regulation. For example, the highly conserved Pumilio family protein FBF-1 represses multiple mRNA targets, thereby maintaining the stem cell potential of germ cells and regulates both their sexual fate as well as the meiotic entry [5]. GLD-1, a STAR-related family member, regulates the fate of several hundred transcripts in the *C. elegans* germ line [6], governs the entry into the meiotic cycle [5] and controls germ cell totipotency [7]. Additionally, we recently showed that GLD-1 cooperates with other conserved RBPs (PUF-8, MEX-3, and CGH-1) to repress CED-3 caspase in specific regions of *C. elegans* germ line [8].

Multiple roles in germ cell development have also been observed with Argonaute proteins in addition to their main role in the RNA interference (RNAi) pathway. For example, *C. elegans* Argonautes ALG-1 and ALG-2 reduce the size of the mitotic germ cell zone and induce an early entry into meiosis [9]. Generally, Argonautes can be subdivided into three clades: the Argonaute clade, which is highly conserved from plants to vertebrates; the PIWI clade, which is conserved in animals; and the nematode-specific Argonaute clade (WAGO) [10]. The majority of the WAGO subgroup is expressed in the germ line and resides mainly in the germline P granules, which localize to the nuclear core complex and enlarge the mRNA transition zone into the cytoplasm [11].

Using an RNAi screen, we have identified the previously uncharacterized RBP C41G7.3 as a novel regulator of apoptosis. C41G7.3 contains three predicted eukaryotic K homology (KH) domains, a 70-amino-acid RNA-binding domain that binds RNA through a very conserved GXXG loop [12]. Since loss of C41G7.3 leads to increased germ cell apoptosis, we termed this gene *mina-1* (messenger RNA-binding inhibitor of apoptosis). In addition to increased apoptosis, *mina-1* mutants display other striking phenotypes, such as proximal cell proliferation, distal oocytes, egg-laying defects, impaired germline integrity, and disorganized and enlarged P granules. Functional and structural characterizations further revealed a genetic and physical association with *wago-4*, the homolog of human Argonaute 1. Our data suggest that *mina-1* and *wago-4* are part of a wider post-transcriptional regulatory network of RBPs that together orchestrate multiple regulatory steps of the germ line to govern differentiation, apoptosis, and RNAi.

Results

Identification of *mina-1*, a novel RBP regulating germline development and apoptosis

We identified the C41G7.3 gene in an RNAi-based screen for genes controlling germline apoptosis [13]. C41G7.3 contains three predicted KH domains, evolutionarily conserved sequences that bind RNA or single-stranded DNA often found in transcriptional and translational regulators [14]. Based on these KH domains, we named the gene *mina-1*.

Apoptosis in the *C. elegans* germ line can be induced by a developmental signal, thought to eliminate supernumerary oocytes [15], as well as in response to stresses, including DNA damage and bacterial infection [16]. The latter pathways are mediated by the BH3 domain protein EGL-1, whereas developmental germ cell death is EGL-1 independent. To characterize the involvement of *mina-1* in germline apoptosis, we analyzed the effects on developmental and DNA-damage-induced germ cell death after *mina-1* RNAi and in the *mina-1* deletion mutant *ok1521*, which lacks exons three to seven of *mina-1*. Both *mina-1(RNAi)* and *mina-1* deletion mutant resulted in strongly increased basal levels of apoptosis and in hypersensitivity to DNA damage-induced apoptosis induced through ionizing radiation (IR) in the *C. elegans* germ line (Figs. 1a–c; Supplementary Figure 1a-d). The *mina-1(ok1521)* apoptotic phenotype was fully rescued by re-expression of green fluorescence protein (GFP)-tagged MINA-1 under the control of its endogenous promoter *opIs408[$P_{mina\text{-}1}$::mina-1::gfp::mina-1(3′-UTR)]* (Fig. 1d, Supplementary Figure 1e).

Increased germline apoptosis induced by loss of *mina-1* was dependent both on the p53 homolog *cep-1* (Fig. 1b) and the checkpoint gene *rad-5* (Supplementary Figure 1f). In particular, we found that the gain-of-function mutation *ced-9(n1950)*, which renders the Bcl-2 homolog CED-9 insensitive to BH3 domain proteins [17], could fully block increased germline apoptosis in *mina-1(RNAi)* animals (Supplementary Figure 1d). Together, these data suggest that loss of *mina-1* function activates a stress-signaling cascade largely dependent on DNA damage response that secondarily induces p53-dependent apoptosis in the *C. elegans* germ line.

Next, we sought to determine the expression pattern of *mina-1*. First, we built a transcriptional reporter *opIs338 ($P_{mina\text{-}1}$::gfp::let-858(3′-UTR)* and found GFP expression under control of *mina-1* promoter throughout the germ line and in oocytes (Supplementary Figure 1g-j). In contrast, using the translational reporter line expressing GFP-tagged MINA-1 *opIs408*, we found that *mina-1::gfp* was expressed only in the transition and pachytene zones (Fig. 1e), suggesting that *mina-1* mRNA might be post-transcriptionally repressed within the mitotic and late meiotic zones. Subcellularly, MINA-1 was localized mainly to perinuclear foci (Figs. 1f–j), which were adjacent to germline P granules (Figs. 1k, l).

In addition to the increased apoptotic levels, *mina-1 (ok1521)* mutants exhibit several other germline defects including frequent presence of hyperploid, oocyte-like cells in the distal and pachytene region of the germ line (Fig. 1m,

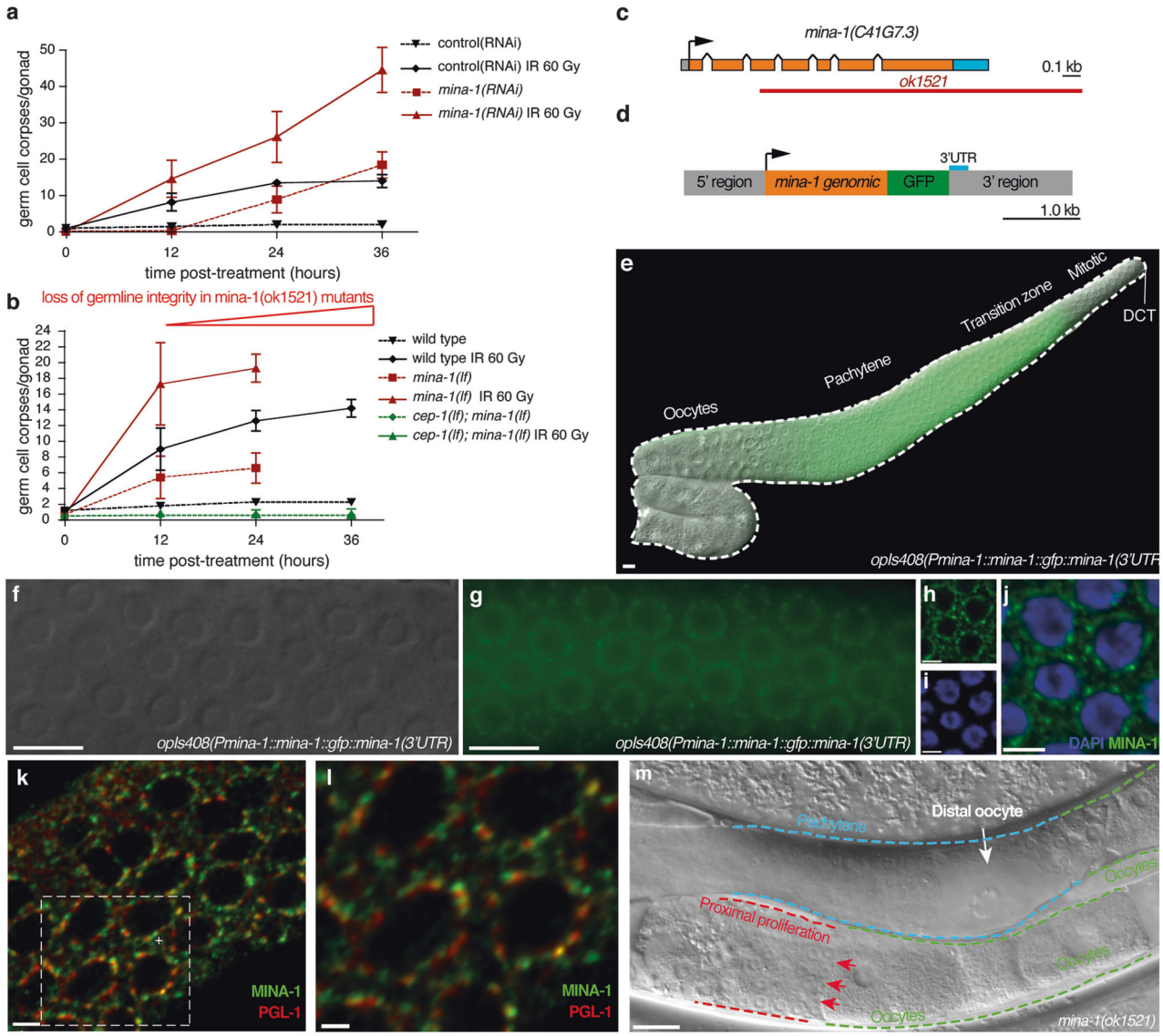

Fig. 1 MINA-1 is a germline-specific protein controlling germ cell development and apoptosis. **a** Synchronized L1 animals were raised on RNAi empty vector control or *mina-1(RNAi)* plates and exposed to IR (60 Gy) as young adults. Germline apoptosis was quantified by DIC microscopy at the indicated time points. Data shown represent the average of three independent experiments ± s.d. ($n > 20$ animals for each experiment and time point). **b** Synchronized wild-type, *mina-1 (ok1521)*, and *cep-1(lg12501);mina-1(ok1521)* young adult animals were irradiated and germline apoptosis was quantified at the indicated time points. Data shown represent the average of three independent experiments ± s.d. ($n > 20$ animals for each experiment and time point). **c** Schematic representation of the *mina-1(C41G7.3)* locus. The *ok1521* allele deletes exons three to seven of the *mina-1* gene. **d** Schematic representation of the MINA-1::GFP fusion construct used to generate the *opIs408* transgene. **e** MINA-1::GFP localization in a composite germline image of a dissected *opIs408*(P_{mina-1}*::mina-1::gfp::mina-1(3′-UTR))* animal. GFP and DIC merged. Scale bars, 10 µm. **f**-**j** DIC (**f**) and fluorescence (GFP channel, **g**) images of germ cells in live *opIs408* animals, and confocal microscopy images of germ cells in fixed *opIs408* animals (**h**: α-gfp antibody to detect MINA-1::GFP (green), **i**: DAPI (DNA, blue), **j**: merge). Scale bars, 10 µm (**f**, **g**), 3 µm (**h**-**j**). **k**, **l** Confocal microscopy images of germ cells in fixed *opIs408* animals using α-PGL-1 antibody (red) as P granule marker and α-gfp antibody to detect MINA-1::GFP (green). **l** is a higher magnification of area indicated in **k**. Scale bars, 2 µm (**k**), 1 µm (**l**). (Note: Pearson's correlation of colocalized volume is between –0.4 and –0.6 for different sections). **m** *mina-1(ok1521)* mutant animals show additional developmental germline defects, including distal oocytes (gogo phenotype: germ cell, oocyte, germ cell, oocyte; white arrow) and proximal proliferation (red arrows). Scale bar, 20 µm

Supplementary Figure 1k-o), a "proximal proliferation" phenotype where mitotic germ cells accumulate between oocytes and spermatheca (Fig. 1m), a general loss of germline integrity (Supplementary Figure 1c, n, o), as well as a reduced rate in progeny production and higher embryonic lethality (Supplementary Figure 1p, q). These observations suggest that loss of MINA-1 disrupts multiple regulatory steps during germline development.

Identification and structure determination of the MINA-1 KH3 domain

MINA-1 contains three regions that fulfill the topological characteristics of eukaryotic KH domains, β1-α1-α2-β2-β'-α', where a highly conserved GXXG motif [12] links helices α1 and α2 and a variable loop connects β2 and β' (Fig. 2a, Supplementary Figure 2a). Matching these criteria with the predicted secondary structure identified residues 12–76, 79–157, and 259–322 as putative KH domains KH1, KH2, and KH3, respectively (Figs. 2a, b). The conserved GXXG loop, which is essential for nucleotide binding [18], deviates in all three putative KH domains from the consensus sequence (Supplementary Figure 2a). In the GXXG loops of KH1 (EPQG) and KH2 (SCTH), at least one glycine is substituted and the common lysine and arginine residues are absent [18, 19]. The GXXG loop of KH3 (GNRA) with an arginine residue and a conservative glycine-to-alanine substitution suggested KH3 as most likely KH domain for RNA binding.

The surprising glycine-to-alanine loop variation in KH3 encouraged us to solve the nuclear magnetic resonance (NMR) structure of MINA-1 (254–334) (Supplementary Figure 2b, Supplementary Table 1), which confirmed the eukaryotic KH domain topology β1-α1-α2-β2-β'-α' (Fig. 2c). Both the GXXG loop containing the GNRA variation and the variable loop of residues 295–303 between β2 and β' are well defined (Fig. 2c). The heteronuclear nuclear Overhauser effect (NOE) experiment revealed a rigid fold for the entire KH3 domain (Supplementary Figure 2c). The rigidity of the GNRA loop contrasts the typically observed dynamics in GXXG loops [19] and may be attributed to the glycine-to-alanine replacement in KH3.

HITS-CLIP identifies *mina-1* target mRNAs and two consensus MINA-1-binding motifs within 3′-UTRs

Based on the confirmed three KH domains, we next sought to determine whether MINA-1 specifically associates with mRNAs. We performed a high-throughput sequencing with crosslinking immunoprecipitation (HITS-CLIP) experiment of synchronized MINA-1::GFP transgenic animals (opIs408) to globally map MINA-1 footprints [20, 21] (Fig. 2d). We identified a total of 563 transcripts to be reproducibly enriched in abundance after applying an expression level cut-off of count per million (cpm) > 1 in all three CLIP replicates and a fold change (FC) > 3 compared with RNA-Seq of MINA-1::GFP animals (Supplementary Table 2). Interestingly, the highest fraction of the identified MINA-1-binding sites mapped to the 3′-UTR of mRNA transcripts with equal distribution throughout the length of the 3′-UTR (Fig. 2e, Supplementary Figure 2d-f), suggesting a possible role in translational regulation or mRNA stability. Applying the multiple expectation maximization for motif elicitation (MEME) algorithm [22] for the 500 most highly enriched "clipped" sites, we identified two closely related *mina-1* consensus binding motifs: UGU-NNN-AU (MBM1) and UGU-NN-AU (MBM2) (Fig. 2f). Intriguingly, MBM1 and MBM2 are very similar to the consensus sequences recognized by PUF-5, PUF-8, FBF-1, and FBF-2, four members of the *C. elegans* pumilio family of RBPs [23, 24].

As HITS-CLIP also identifies interactions that may be transient [25], we also used ribonucleoprotein immunoprecipitation followed by microarray (RIP-Chip) as a complementary method to identify transcripts that are stably associated with MINA-1. Out of 10,805 transcripts that were detected on the array, 796 transcripts were at least twofold enriched in MINA-1 compared with control HUS-1 IPs (a DNA damage checkpoint protein widely expressed in the germ line) (Supplementary Table 3). In all, 430 (76.4%) of the 563 MINA-1 HITS-CLIP targets could also be quantified in the RIP-Chip experiment. Among them, 94 were found to be enriched in the MINA-1 IP, whereas only 3 were enriched in the HUS-1 control IP (Fig. 2g). Furthermore, the 430 MINA-1 HITS-CLIP targets were significantly enriched compared with non-target transcripts (Fig. 2h), suggesting that a significant fraction of the MINA-1 HITS-CLIP target set are *bona fide* targets.

Determination of the interaction surface of MINA-1 (254–334) with its target RNA

Given that the interactions between MBM1/MBM2 and MINA-1 (254–334) were not sufficiently tight to solve the structure of the complex, we next analyzed the interaction surface of MINA-1 (254–334) with the tighter binding MBM2 RNA. We performed an NMR titration series of ^{15}N-labeled MINA-1 (254–334) with cUGUGAAUa MBM2 RNA that contains an additional C and A nucleotide at the ends to mimic an internal RNA motif at the binding site (Supplementary Figure 3a). The amide resonances of the residues contacting the RNA were in fast to intermediate exchange on the NMR timescale, which agrees with the determined K_d of ca. 16 μM (Supplementary Table 4). Investigation of the combined ^{1}H and ^{15}N chemical shift perturbations (CSP) upon RNA binding (Supplementary Figure 3c) indicates a strong contribution of the GNRA loop of MINA-1 (254–334) to the protein–RNA interaction (Fig. 2i), which is the first report of a KH domain with an altered GXXG loop sequence that shows direct nucleic acid-binding activity [18]. In fact, any deviation of the highly conserved GXXG loop from the consensus sequence was considered as exclusion criterion for direct RNA-binding activity [18, 19]. Further perturbations were observed in helices α1 and α2, the variable loop between β2 and β', and

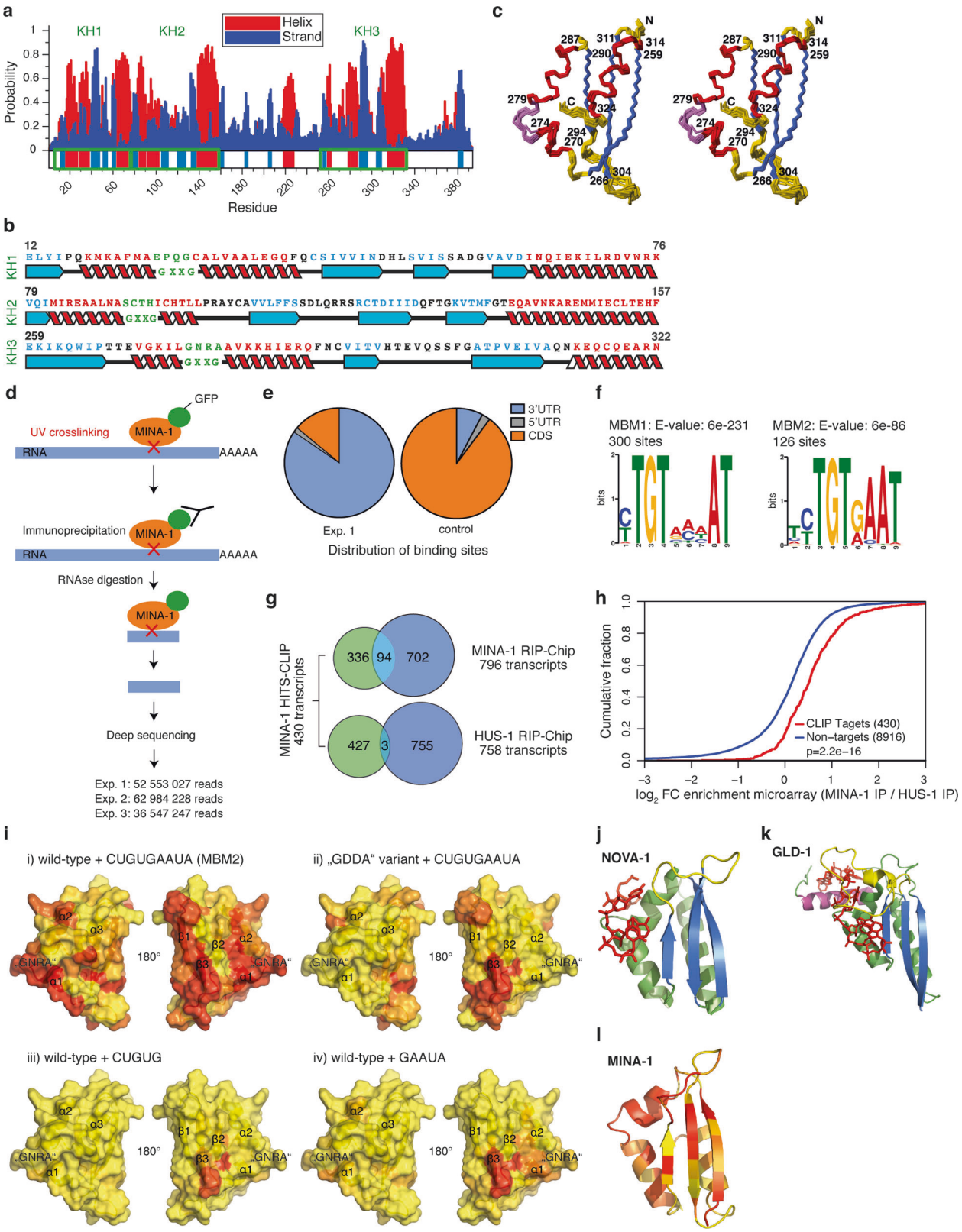

β-strands β2 and β' (Fig. 2i, Supplementary Figure 3c). The unusual perturbations in β-strand β1 could be attributed to an increased interaction surface in this particular KH domain that enables accommodation of longer RNA sequences: KH domains typically recognize four nucleotides via their canonical nucleic acid-binding surface

◀ **Fig. 2** MINA-1 has a KH3 domain with a non-canonical "GNRA" loop essential for RNA binding and binds to target 3′-UTRs mainly via two related binding motifs. **a** Secondary structure prediction of MINA-1 using the JUFO neural network algorithm. Putative KH domains are indicated by KH1, KH2, and KH3. The probability of α-helical (red bars) and β-strand (blue bars) secondary structure elements is plotted against the sequence of MINA-1. **b** Sequence and predicted secondary structure elements of the three putative KH domains of MINA-1. Eukaryotic KH domains are characterized by β1-α1-α2-β2-β'-α' topology and a "GXXG" loop (in green), which is located between helices α1 and α2, which is essential for RNA binding. The predicted α-helices and β-strand are indicated with red and blue colors, respectively. **c** Stereoview of the 20 lowest-energy conformers representing the solution structure of the KH3 domain of MINA-1 after energy-minimization with AMBER. The sequence boundaries of α-helical (red) and β-stranded (blue) regions are shown; magenta bonds indicate the "GNRA" loop. PDB deposition ID: 6FBL. **d** Overview of the high-throughput sequencing of RNA isolated by crosslinking immunoprecipitation (HITS-CLIP) of MINA-1::GFP and control. Synchronized young adult opIs408 animals were exposed to UV light to cross-link RNAs and proteins in situ. Cross-linked RNA was co-purified with MINA-1::GFP and subjected to RNA sequencing. Displayed are also the reads achieved in each of the three independent experiments [20, 21]. **e** Pie charts show the distribution of the binding sites in the 3′-UTR (blue), 5′-UTR (gray), and CDS (orange) of sequenced RNAs of control (total RNA-Seq) and first experiment. **f** Consensus MINA-1-binding motifs (MBM) identified by HITS-CLIP. MBM1 is present in 300 and MBM2 in 126 of the top MINA-1 500 binding sites, respectively. **g** Venn diagrams show overlap of transcripts enriched in MINA-1 CLIP (430 transcripts) and in MINA-1 RIP-Chip (796 transcripts) or HUS-1 RIP-Chip (control, 758 transcripts) experiments. Regarding the RIP-Chip experiments, transcripts that were at least twofold enriched ($\log2 > 1$) in either IPs were further considered. The CLIP dataset consists of transcripts enriched compared with RNA-seq of young adults expressing MINA-1::GFP with applying a filter of detection of 1 cpm in all three CLIP replicates. In all, 94 genes overlapped between MINA-1 CLIP and MINA-1 RIP-Chip (P-value $= 1.05 \times 10^{-22}$). **h** Cumulative fraction analysis of fold change distribution ($\log_2$) of CLIP targets and non-targets. P-values were calculated with the Kolmogorov–Smirnov (KS) test. **i** Surface representation of MINA-1 residues 257–331 showing the combined ^{1}H and ^{15}N chemical shift perturbation (CSP) upon titration of wild-type MINA-1 with (i) CUGUGAAUA-RNA, (iii) CUGUG-RNA, and (iv) GAAUA-RNA and upon titration of the (ii) "GDDA" MINA-1 variant with CUGUGAAUA-RNA. The color coding reflects the gradient of the observed perturbations, ranging from yellow (no CSP) to red (CSP ≥ 0.1). **j** KH domains typically recognize up to four nucleotides via their canonical nucleic acid-binding surface comprising helices α1 and α2, the GXXG and variable loops and β-strand β2, which is exemplified by the complex of NOVA-1 with UCAC-RNA. **k** The specific recognition of longer target sequences requires domain extensions such as the additional α-helix provided by the QUA2 domain in GLD-1. **l** The MINA-1 KH3 domain preferentially binds to longer target RNAs by additional involvement of β-strands β1 and β'. Color-coding of a cartoon representation of the KH3 domain according to the CSP upon binding of the KH3 domain to the CUGUGAAUA-RNA

comprising helices α1 and α2, the GXXG and variable loops and strand β2 [18, 26] (Fig. 2j). Recognition of longer RNA sequences requires domain extensions such as the additional α-helix contributed from the QUA2 domain in GLD-1 [27] (Fig. 2k). To investigate whether KH3 indeed specifically recognizes longer target RNA sequences, we performed separate NMR titrations of MINA-1 (254–334) with CUGUG and GAAUA RNAs that resemble the 5′- and 3′-halves of the CUGUGAAUA oligonucleotide, respectively (Supplementary Figure 3b, c). Titration with the 5-mer RNAs induces significantly weaker perturbations for residues in strands β1 and β', which supports the potential involvement of these elements in accommodation of the longer CUGUGAAUA RNA (Fig. 2i, Supplementary Figure 3b). The perturbations of helices α1 and α2 and the GNRA loop are also significantly reduced, which agrees with a weakened interaction of the 5-mer RNAs compared with the 9-mer RNA (Supplementary Figure 3c). These observations indicate that the KH3 domain of MINA-1 preferentially accommodates longer RNA sequences without the requirement of domain extensions as seen with KH domains of the signal transduction and activation of RNA (STAR) protein family [27].

Characterization of an RNA-binding GDDA mutant of MINA-1 (254–334)

The atypical GNRA loop in MINA-1 (254–334) is the first example of an actively RNA-binding KH domain without the consensus GXXG loop. To examine the role of the GNRA loop in the recognition of target RNA, we mutated GNRA into a GDDA loop since negatively charged residues in the GXXG loop are known to prevent RNA binding [19]. NMR assignment of the GDDA-MINA-1 (254–334) variant revealed nearly identical resonances as in the wild-type variant, which suggests the same native fold for the GDDA variant and the wild-type KH3 domain (Supplementary Figure 3d, e). The largest deviations between the wild-type and the GDDA variants are clustered around the site of mutation, as expected. We then performed NMR titrations of the GDDA-KH3 variant with the 5-mer GAAUA-RNA and observed weak but significant perturbations for residues His295, Glu297, and Val298 of the variable loop region between β-strands β2 and β' (Supplementary Figure 3d), indicating weak RNA interactions even in absence of a functional GXXG loop. Subsequent titration of the GDDA variant with the 9-mer CUGUGAAUA-RNA caused even more pronounced perturbations in those variable loop residues and further perturbed residues that showed no involvement in binding to the 5-mer RNA (Fig. 2i, Supplementary Figure 3e). This suggests preferential binding of the longer 9-mer RNA even without the contribution of the GNRA loop, and suggests a secondary RNA-binding site for accommodation of longer RNA sequences. Direct comparison of the titrations of wild-type and GDDA variant with the 9-mer RNA reveals decreased perturbations in the binding loop region of the GDDA variant, as expected (Supplementary Figure 3f). However, the pronounced

perturbations for residues in β-sheets β1 and β2 in the GDDA variant support the presence of a secondary RNA interaction site that contributes to the preferential binding of longer RNA in the wild-type protein. This secondary binding site appears to be located around the variable loop and β-strands β1, β' and β2 and includes a His and a Trp residue that could provide stacking interactions to the bases of the target RNA (Supplementary Figure 3g). The combination of the primary RNA-binding site comprised of helices α1 and α2, the GNRA and variable loop with the secondary binding site that includes the variable loop and the antiparallel β-sheets should provide a sufficiently large interaction surface to accommodate longer target RNAs without the need for domain extensions (Fig. 2l).

WAGO-4 protein and mRNA are upregulated in *mina-1* mutants

To determine which MINA-1 targets might contribute to the various *mina-1* phenotypes, we explored the consequences of *mina-1* loss at transcriptome and proteome levels. First, we compared protein abundance in wild type and *mina-1(ok1521)* animals using stable isotope labeling by amino acids (SILAC) (Supplementary Figure 4a). Of the 1323 proteins quantified in two biological replicates, only seven proteins (WAGO-4, NCS-2, CASH-1, MPPA-1, FAR-3, D1054.11, and C08B11.9) were more abundant and three (Y41C4A.11, GLRX-21, TAG-151) were less abundant in *mina-1* mutant (Fig. 3a). Interestingly, the most abundant protein was the worm Argonaute family member WAGO-4.

Next, we analyzed changes at mRNA level in *mina-1* mutants. Of a total of 12,861 genes quantified, 56 transcripts were upregulated and 73 downregulated, using a cut-off of ± 0.7 $\log_2$-FC and adjusted *P*-value < 0.1 (Fig. 3b, Supplementary Table 5). Interestingly, gene ontology term analysis using DAVID [28] of the upregulated genes yielded an enrichment of genes in the category "RNA-binding", including genes such as *fbf-1*, *fbf-2*, *glh-1*, and *nos-3*. In contrast, seven genes involved in life span determination were overrepresented among the downregulated genes in *mina-1* mutants (Supplementary Table 6). Congruently with the above protein abundance results, *wago-4* was also found to be significantly upregulated at mRNA level in *mina-1* mutant.

To compare SILAC and transcriptome profiling, we performed a correlation analysis between protein and mRNA abundance changes. Although the correlation coefficient was low ($r = 0.188$) (Fig. 3c), we confirmed that the worm Argonaute *wago-4* showed the strongest and most consistent change at both mRNA and protein levels (2.6-fold and 4.3-fold upregulation, respectively). Taken together with the fact that WAGO-4 is also enriched in our MINA-1 CLIP and RIP-Chip data (Supplementary Table 2, 3), these data suggest MINA-1 as an important regulator of WAGO-4.

We then investigated the effects of the loss of *mina-1* function on mRNA of its 474 CLIP targets, for which we had transcript abundance data. This comparison revealed that target mRNA expression is generally increased in *mina-1* mutants compared with non-target transcripts, hinting at a possible role of MINA-1 in target mRNA destabilization (Supplementary Figure 4b). A similar comparison with the 30 clipped targets quantified at the protein level also showed a trend towards target upregulation in *mina-1* mutants (Supplementary Figure 4c). Additional comparison of MINA-1 CLIP enrichment with FCs in protein and mRNA abundances in *mina-1* mutant revealed that transcripts harboring top clipped sites showed a better correlation with protein ($r > 0.25$) than with mRNA FCs ($r < 0.2$), suggesting that the top clipped targets are regulated mainly at the translational level. However, a considerable number of transcripts correlated with mRNA FCs and showed no correlation with translation efficiency, implying an additional role of MINA-1 in mRNA destabilization (Supplementary Figure 4d).

MINA-1 regulates its own mRNA and an RBP cluster involved in gene silencing, maintaining stem cell proliferation, and meiotic entry

To identify biologically relevant MINA-1 targets, we focused on the MINA-1 HITS-CLIP targets, which showed at the same time a significant change in protein and/or mRNA abundance compared with *mina-1* mutant, or were enriched in MINA RIP-Chip experiment (Figs. 3d–f). In addition to WAGO-4, these datasets contained a large number of additional germline RBPs, including the PUF family members FBF-1 and FBF-2, another Argonaute protein called PPW-2, and the KH domain protein GLD-1. Analysis of the MINA-1-binding sites showed that not only *mina-1* mRNA but also the transcripts of all five genes contained one or several MBSs, which were located within their 3′-UTRs (Fig. 3g, Supplementary Figure 5a-c), consistent with the hypothesis that they are direct targets of MINA-1.

MINA-1 binding of the *fbf-1* transcript is very interesting considering its expression patterns. FBF-1 was shown to be expressed in the mitotic region, where it maintains germline stem cells and its expression is rapidly reduced upon entry into the early meiotic prophase. This is consistent with a possible repression by MINA-1, as MINA-1 expression starts exactly at that point (Fig. 1e). If MINA-1 indeed inhibits *fbf-1* via its 3′-UTR, then loss of MINA-1 function should lead to an increase in expression in an *fbf-1* 3′-UTR-dependent manner. Indeed, we found that loss of *mina-1* function strongly increased GFP expression in a strain

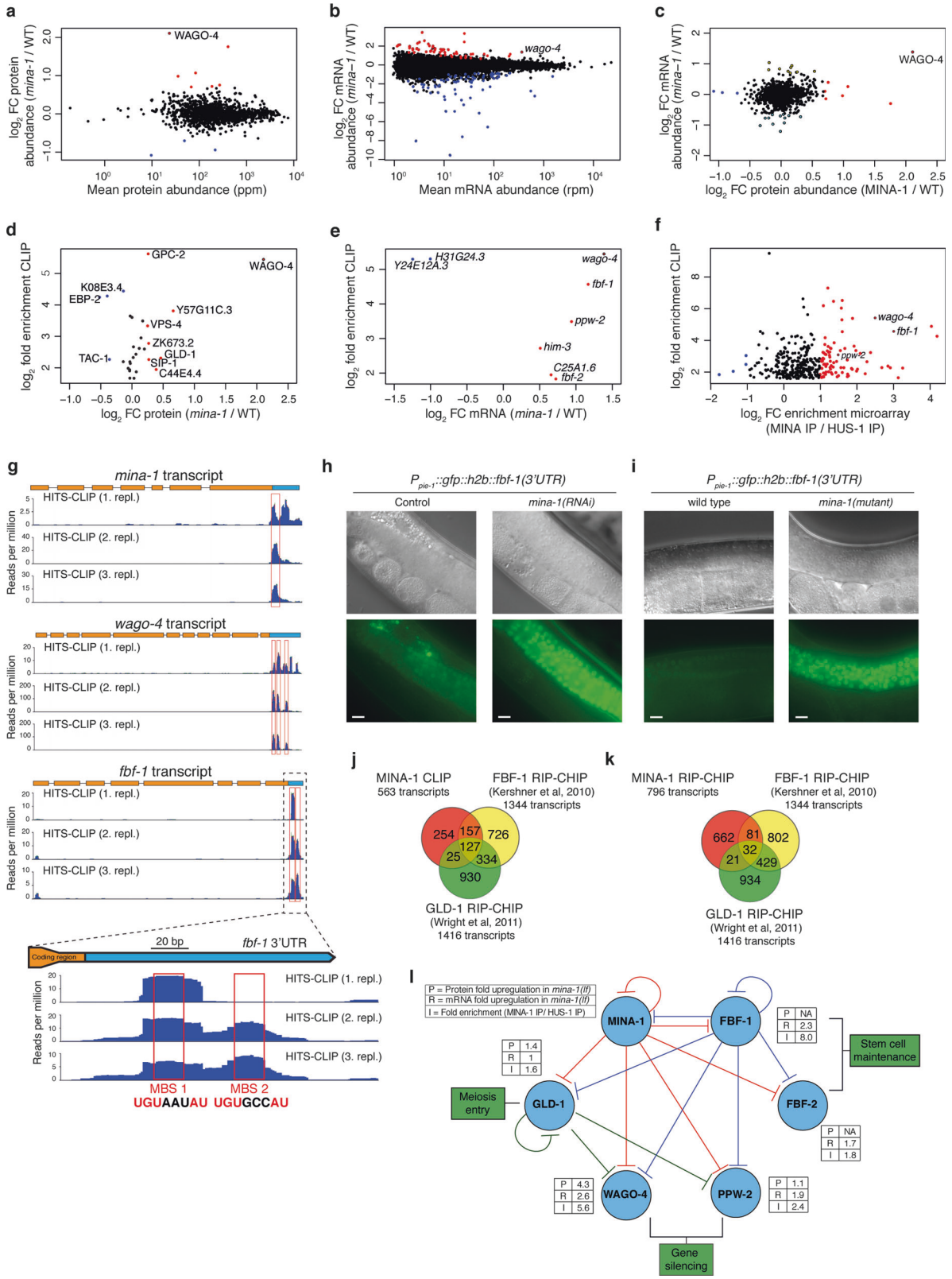

expressing GFP::H2B under the control of the endogenous *fbf-1* 3′-UTR [29] (Fig. 3h, i), in keeping with the notion that MINA-1 represses *fbf-1*. By contrast, analysis of germ cell apoptosis in *mina-1(ok1521); fbf-1(ok91)* showed that absence of *fbf-1* did not rescue the increased germline apoptosis of *mina-1* mutants (Supplementary Figure 5d),

◀ **Fig. 3** MINA-1 regulates its own mRNA and an RBP cluster. **a** Relative protein abundance in *mina-1* mutants and wild type were quantified by SILAC in two biological replicates. Overall mean protein abundance was extracted from the integrated *C. elegans* PaxDB dataset [1]. Upregulated (log_2 fold change (*mina-1*/WT) ≥ 0.7) and downregulated proteins (log_2 fold change (*mina-1*/WT) ≤ -0.7) are marked with red and blue dots, respectively. **b** Relative mRNA expression in *mina-1* mutants and wild type was quantified by RNA-seq in three biological replicates. Upregulated (log_2 fold change (*mina-1*/WT) ≥ 0.7; *P*(adj) < 0.1)) and downregulated transcripts (log_2 fold change (*mina-1*/WT) ≤ 0.7; *P*(adj) < 0.1) are marked with red and blue dots, respectively. **c** Comparison of protein to mRNA changes (log_2 fold change (*mina-1*/WT)) of 1294 genes whose abundance was quantified in both SILAC and RNA-seq experiments. Upregulated (log_2 fold change (*mina-1*/WT) ≥ 0.7) and downregulated proteins (log_2 fold change (*mina-1*/WT) ≤ -0.7) are marked with red and blue dots, respectively. Upregulated (log_2 fold change (*mina-1*/WT) ≥ 0.7) and downregulated transcripts (log_2 fold change (*mina-1*/WT) ≤ -0.7) are marked with yellow and light blue dots with a black border, respectively. **d**, **e** Comparison of log_2 fold change enrichments of a subset of MINA-1 CLIP targets at the protein (**d**) and mRNA (**e**) levels. All MINA-1 CLIP targets that were quantified at the protein level (log_2 fold change (*mina-1*/WT) ≥ 0.2 or ≤ –0.2) are shown in **d** (upregulated in red and downregulated in blue), whereas **e** only includes upregulated (red) and downregulated (blue) targets that showed a significant difference (*P*(adj) < 0.1) in mRNA abundance between *mina-1* mutant and wild type. **f** Graph shows log_2 fold change enrichment in HITS-CLIP and microarray (MINA-1 IP/HUS-1 IP) of CLIP targets. Transcripts significantly enriched (as defined in Fig. 2f) in MINA-1 IP and control HUS-1 IP are marked with red and blue dots, respectively. **g** Visualization of MINA-1 HITS-CLIP signal in the 3′-UTR (marked in blue) of *mina-1*, *wago-4*, and *fbf-1* transcripts. Number of reads per million from the HITS-CLIP experiment along the transcript are shown. Sites where accumulation of reads correspond to one of the two consensus motifs (MBM1 or MBM2) are marked with red boxes. The *fbf-1* 3′-UTR is additionally zoomed to show the 2 MBM-containing sites (MBS1–2). **h** DIC and fluorescence images of the reporter line $P_{Pie\text{-}1}$*::gfp::h2b::fbf-1(3′-UTR)* after control (empty vector) and *mina-1* RNAi. Scale bars, 10 µm. **i** DIC and fluorescence images of the reporter line $P_{Pie\text{-}1}$*::gfp::h2b::fbf-1(3′-UTR)* in wild type and *mina-1* mutant. Scale bars, 10 µm. **j** Venn diagram showing the overlaps between MINA-1 CLIP targets and targets identified in FBF-1 (1344 targets, SAM > 0.965) and GLD-1 (1416 targets, fold enrichment > 2) RIP-CHIP experiments [6, 24]. In all, 284 genes overlapped with FBF-1 RIP-Chip (*P*-value = 7.9×10^{-74}) and 152 with GLD-1 RIP-Chip (*P*-value = 1.9×10^{-25}). **k** Venn diagram showing the overlap between MINA-1 RIP-Chip targets and targets identified in FBF-1 and GLD-1 RIP-CHIP experiments [6, 24]. In total, 113 overlapped with FBF-1 RIP-Chip (*P*-value = 4.4×10^{-6}) and 53 with GLD-1 RIP-Chip (n.s.). **l** Network showing the post-transcriptional regulatory interactions between MINA-1 and several RBPs including WAGO-4, FBF-1, FBF-2, GLD-1, and PPW-2. Target protein (P) and mRNA (R) upregulation in *mina-1* mutants as well as MINA-1 RIP-CHIP enrichment (I) are shown. Red, blue, and green lines represent regulation by MINA-1 FBF-1, and GLD-1, respectively

suggesting that increased germline apoptosis of *mina-1* mutants is not dependent on FBF-1 overexpression.

Next, we compared MINA-1 HITS-CLIP and RIP-Chip data with published data from GLD-1 [6] and FBF-1 [24] immunoprecipitation experiments. Of the 563 MINA-1 CLIP targets, 353 (62.3%) and 327 (58.1%) were represented in FBF-1 and GLD-1 RIP-Chip data, respectively. Among these, we identified 284 and 152 targets to be shared with the FBF-1 and GLD-1 RIP-Chip enriched targets. Of the 796 MINA-1 RIP-Chip targets, on the other hand, 227 (28.5%) and 263 (33%) were represented in FBF-1 and GLD-1 RIP-Chip, respectively. Only 113 and 53 transcripts were identified to overlap with FBF-1 and GLD-1 RIP-Chip datasets (Figs. 3j, k).

Interestingly, several of the MINA-1 target RBPs were also targeted by FBF-1 and/or GLD-1. For example, the analysis of GLD-1 HITS-CLIP [30] and PAR-CLIP [31] datasets identified strong and reproducible GLD-1 binding sites in *wago-4* and *wago-3* 3′-UTRs (Supplementary Figure 5e-g). In addition to *wago-4* and *wago-3*, FBF-1 RIP-Chip-associated probe set [24] also includes *mina-1* and the previously characterized targets *gld-1* [32] and *fbf-2*.

Together, these data suggest that MINA-1, FBF-1, FBF-2, WAGO-4, GLD-1, and PPW-2 might constitute an RNA regulon [2, 33], which coordinately regulates stem cell proliferation, gene silencing (see below), meiotic entry, and apoptosis via RBPs (Fig. 3l).

MINA-1 interacts with the Argonaute protein WAGO-4 to co-regulate RNAi

Most RBPs form dynamic complexes with other proteins at different stages of their life cycle to regulate RNA metabolism [34]. To investigate protein interacting partners of MINA-1, we immunoprecipitated MINA-1 from a transgenic line expressing the MINA-1::GFP reporter and identified co-enriched proteins by mass spectrometry. Strikingly, WAGO-4 co-immunoprecipitated with MINA-1 in all three biological replicates but not in negative controls (Fig. 4a, Supplementary Table 7). Taken together with our previous observations on the regulation of *wago-4* mRNA and protein levels by MINA-1 and MINA-1 binding to the *wago-4* 3′-UTR, these results reinforce the functional link between MINA-1 and WAGO-4.

Many Argonaute family members are involved in the RNAi pathway. Loss-of-function of these RNAi components in *C. elegans* can lead to a resistance phenotype against exogenous RNAi. Such mutants, as in the case of the Argonaute RDE-1, are unresponsive to RNAi after introduction of double-strand RNA (dsRNA) [35]. Given that WAGO-4 contains the canonical PIWI and PAZ domains typical of Argonaute proteins (Figs. 4b–d), we analyzed the effect of *wago-4* knockout on the activity of the RNAi machinery. We performed a series of RNAi experiments targeting genes expressed either in the soma (*unc-15* and *unc-52*) or in the germ line (*gld-1*, *pos-1*). Interestingly, we found that *wago-4* mutants showed a strongly germline-specific insensitivity to RNAi (Figs. 4e, f). The RNAi deficiency phenotype was completely rescued

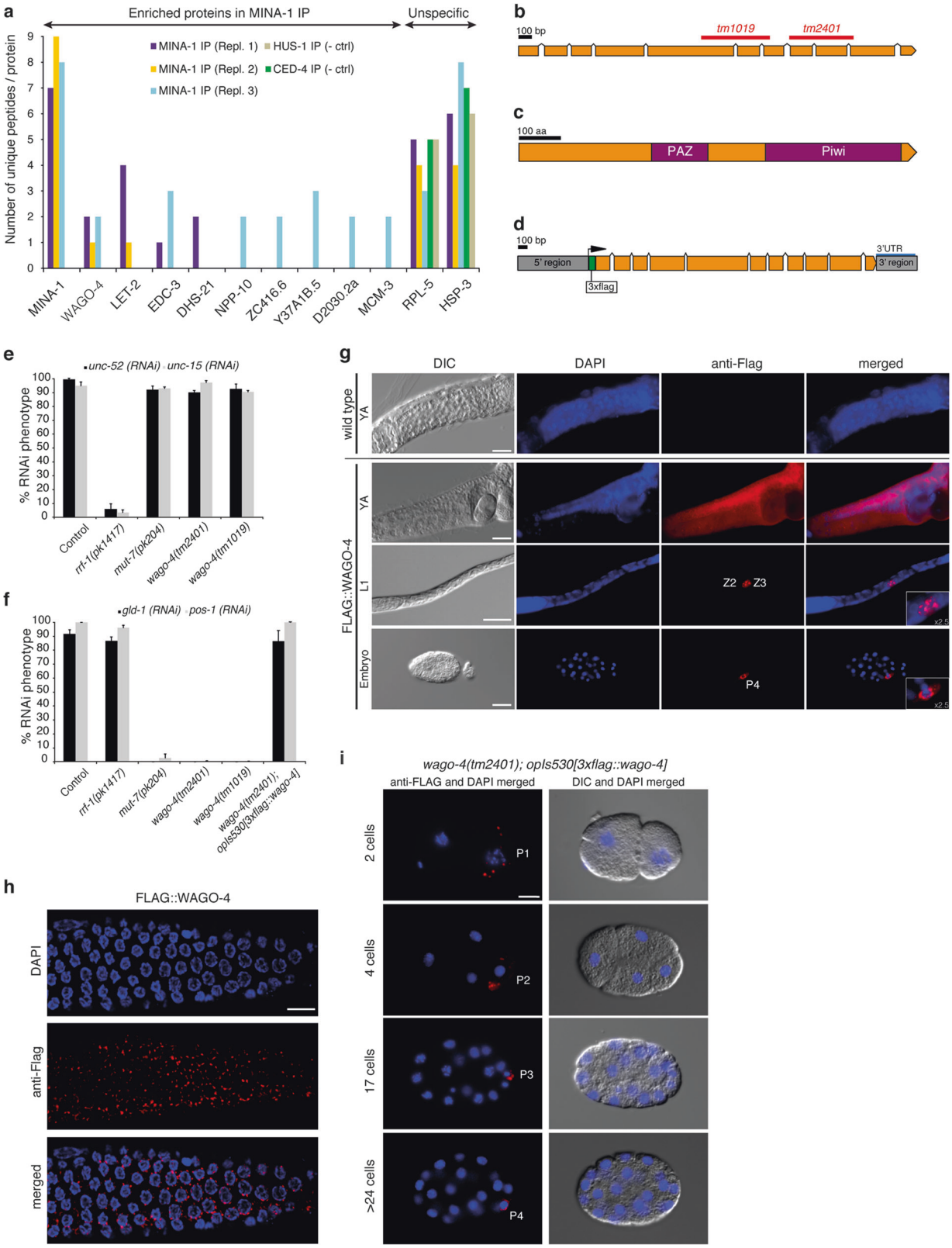

in the *opIs530[3xflag::wago-4]* transgene, which reintroduces a flag-tagged wild-type copy of *wago-4* (Fig. 4f). These results show that WAGO-4 is required for effective RNAi in the *C. elegans* germ line.

Congruently, flag-tagged WAGO-4 showed a germline-specific localization throughout the entire animal's life cycle. In young adult worms, the signal was uniformly present over the entire gonad, starting from the distal tip,

◀ **Fig. 4** MINA-1 interacts with the Argonaute protein WAGO-4 to co-regulate RNAi. **a** Protein co-immunoprecipitation on worms expressing MINA-1::GFP detected WAGO-4 in all three replicates and none of the control IPs. Eluates after the IP were ran on SDS-PAGE gel, cut out, digested and peptides analyzed by Orbitrap Mass Spectrometer. Proteins expressed in the meiotic region of the germ line: CED-4 and HUS-1 were used as a control. Protein threshold of 99% was used and minimum number of peptides used to identify a protein was set to 1. The number of unique peptides detected per protein is displayed on the chart. **b** Schematic representation of the *wago-4(F58G1.1)* locus, including the two deletions *tm1019* and *tm2401*. **c** Schematic representation of the WAGO-4 protein and its two Argonaute domains PAZ and Piwi (purple). **d** Schematic representation of the 3xFLAG::WAGO-4 fusion construct used to generate the *opIs530[3xflag::wago-4]* transgene. The 5′ region (gray) is 841 bp long, followed by a 3xflag tag (green) and the *wago-4* gene (orange). After the STOP codon, a 486 bp 3′ region (blue) completes the transgene, which was inserted on Chromosome IV via MosSCi. **e**, **f** Somatically expressed genes (**e**, *unc-52*, *unc-15*) and germline-specific genes (**f**, *gld-1*, *pos-1*) were knocked down in wild type, *rrf-1(pk1417)*, *mut-7(pk204)*, *wago-4 (tm1019)*, and *wago-4(tm2401)* mutants. Related phenotypes were quantified in three independent experiments. The transgene *opIs530 [3xflag::wago-4]* rescues the tissue-specific RNAi resistance of *wago-4(tm2401)* mutants (**f**). **g** Immunostaining of transgenic *opIs530 [3xflag::wago-4]* and wild-type worms. DIC, DNA(DAPI, blue), anti-Flag(red), and merged channels show expression of FLAG-tagged WAGO-4 in the adult germ line and its precursor cells (Z2, Z3 in L1 worms, and P4 in the embryo). Inserts show a zoomed view of the germ line precursor cells. Scale bars, 20 µm. **h** Confocal image of a dissected *opIs530[3xflag::wago-4]* young adult germ line stained with anti-FLAG (red) and DAPI (blue). Scale bar, 20 µm. **i** P lineage affiliated expression of transgene *opIs530[3xflag::wago-4]* in *wago-4* mutant background in 2, 4, 7, and 16 cells stage. Left column represents the merged channels of DNA (DAPI, blue) and WAGO-4 (anti-FLAG, red). Right column represents corresponding DIC images of the cells. Scale bar, 10 µm

passing through the mitotic and pachytene zone, and ending in the area were oogenesis takes place (Fig. 4g). A closer view of the gonad showed that 3xFLAG::WAGO-4 signal was distributed as round electron-dense structures around germ cells nuclei (Fig. 4h). As previously shown [36], we also found that WAGO-4 signal segregates asymmetrically to the germline precursor cells P1–P4 during early embryogenesis (Fig. 4i).

The punctate, perinuclear localization of WAGO-4 led us to investigate their possible association with P granules. Similar to our observations on MINA-1 localization next to P granules, WAGO-4 was previously found to localize to an independent liquid-like condensate termed Z granules, which is adjacent to P granules, supporting the idea that WAGO-4 might only be a transient P granule member [36] (Supplementary Figure 6a-c).

MINA-1 negatively regulates WAGO-4 to control apoptosis, RNAi efficiency, and P granules organization

Our proteomics analysis has shown an up to fourfold upregulation of WAGO-4 protein in *mina-1* mutants (Fig. 3a) an observation, which we confirmed by western blot (Fig. 5a). Increased expression of 3xFLAG::WAGO-4 in the absence of MINA-1 was also readily detectable by immunocytochemistry (Fig. 5b).

Loss of WAGO-4 function did not result in any overt developmental defect on its own, but strongly suppressed the reduction in the rate of egg laying and in total brood size (Figs. 5c, d), as well as the increased germ cell apoptosis in *mina-1* mutants (Fig. 5e). These results suggest that a significant fraction of the defects observed in *mina-1* mutants might be due to overexpression of WAGO-4, identifying WAGO-4 as a key functional target of MINA-1.

To strengthen this hypothesis, we analyzed the effects of WAGO-4 overexpression in *mina-1* mutant on the effectiveness of RNAi. We performed RNAi experiments of *gld-1* and *pos-1* in wild type and *mina-1(ok1521)* with different isopropyl-beta-D-thiogalactopyranosid (IPTG) concentrations, enabling the induction of a varying response to RNAi. Indeed, we found that *mina-1* mutants showed a significantly greater sensitivity to RNAi (Figs. 5f, g). Taken together, these results suggest a central role for MINA-1 in the modulation of the RNAi response through WAGO-4 in the *C. elegans* germ line.

In wild-type germ cells, P granules are fairly homogeneous in size and surround the nucleus in a highly organized manner, observable both under light microscopy and transmission electron microscopy (TEM; Figs. 5h–l, Supplementary Figure 7a). In *mina-1* mutant germ cells, P granules were often enlarged and asymmetrically distributed (Figs. 5i–p, Supplementary Figure 7b). The average P granule base length in *mina-1* mutants as measured in TEM sections was about 1.3 times longer than the wild-type P granule base length (Fig. 5q).

Is overexpression of WAGO-4 responsible for the enlargement of P granules in *mina-1* mutants? P granules are slightly smaller but evenly distributed in *wago-4 (tm2401)* mutants (Figs. 5j–q, Supplementary Figure 7c). Interestingly, we observed the same phenotype in the *mina-1(ok1521); wago-4(tm2401)* double mutants, indicating that loss of *wago-4* function suppresses the P granule defect of *mina-1(ok1521)* mutants (Figs. 5k–q, Supplementary Figure 7d). In summary, we conclude that loss of MINA-1 results in a WAGO-4 overexpression-dependent alteration of the P granule architecture.

Discussion

In this study, we describe MINA-1 as a novel germline-specific RBP. MINA-1 functions in the germline pachytene zone, where it closely interacts with the Argonaute protein WAGO-4 and cooperatively governs germline differentiation, apoptosis, and RNAi.

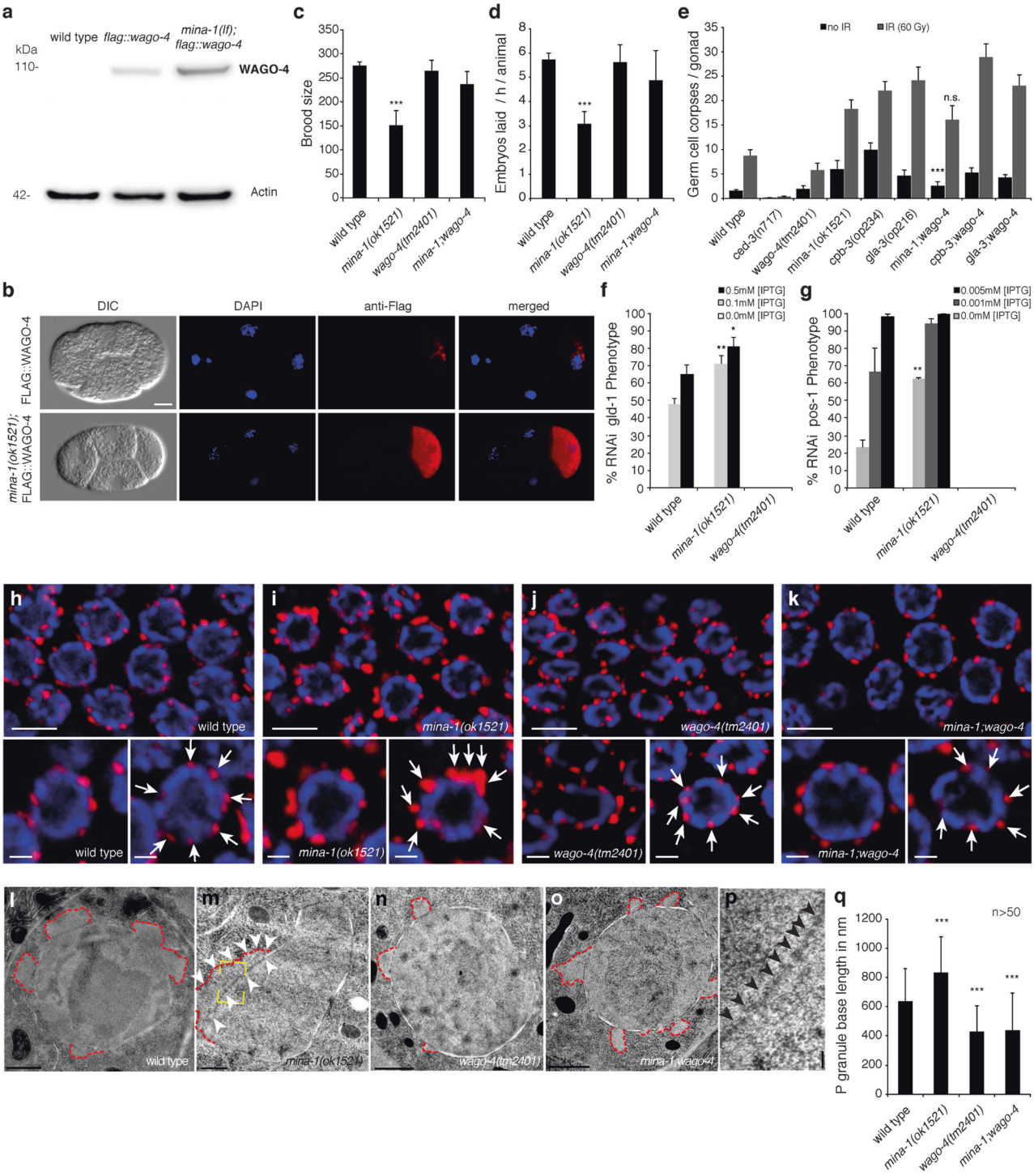

We explored the mechanism of action of MINA-1 and its targets, which are relevant for the apoptotic phenotype, by integrating system-wide proteome and transcriptome profiling, HITS-CLIP, RIP-CHIP, and protein–protein interaction data. We found that MINA-1 overall destabilizes target mRNAs and represses translation. Specifically, we show that MINA-1 negatively regulates the *wago-4* protein and mRNA levels—irrespective of the observed upregulation of other RBPs in *mina-1* mutants, which also bind to *wago-4* mRNA and are known to repress their target expression [30]. Moreover, WAGO-4 co-precipitated with MINA-1, suggesting a potential protein–protein interaction. Importantly, we demonstrated that interaction between MINA-1 and WAGO-4 and deregulation of WAGO-4 in *mina*-1 mutants is functionally relevant for the regulation of germ cell apoptosis levels and RNAi efficacy (Figs. 6a–c).

◀ **Fig. 5** MINA-1 negatively regulates WAGO-4 to control apoptosis, RNAi efficiency, and P granule organization. **a** Representative western blot image of 3xFLAG::WAGO-4 (detected using an anti-FLAG antibody) and actin (ACT-5) in whole animal extracts of wild-type, *opIs530[3xflag::wago-4]*, and *mina-1(ok1521); opIs530[3xflag::wago-4]* staged young adults. **b** Immunostaining of *opIs530[3xflag::wago-4]* and *mina-1(ok1521); opIs530[3xflag::wago-4]* four-cell stage embryos. In a wild-type background, 3xFLAG::WAGO-4 shows a punctate perinuclear staining (blue: DAPI, red: anti-FLAG); this staining increases in intensity and spreads out throughout the cytoplasm in *mina-1(ok1521)* mutants. Scale bar, 10 µm. **c**, **d** Determination of brood size and embryos laid per hour per animal in wild type, *mina-1(ok1521)*, *wago-4(tm2401)*, and *mina-1(ok1521); wago-4(tm2401)* mutants. Data shown are average ± standard deviation of three biological replicates ($n = 20$ animals/experiment). *P*-values were calculated using Student's *t*-test: $^{***}P < 0.001$. **e** Synchronized animals were scored for germ cell apoptosis 24 h post L4 larval stage/adult molt with (gray) and without (black) IR (60 Gy). Data shown are average ± standard deviation of five biological replicates ($n = 20$ animals/experiment). *P*-values were calculated using Student's *t*-test: $^{***}P < 0.001$, n.s. not significant. **f**, **g** Dose-response RNAi knockdown of *gld-1* (**f**) and *pos-1* (**g**) in wild-type, *mina-1 (ok1521)*, and *wago-4(tm2401)* animals, using three IPTG concentrations (0 mM, 0.1 mM, and 0.5 mM). Data shown are averages ± standard deviation of three (**p**, 25 animals each) and two (**q**, 10 parents each) biological replicates. *P*-values were calculated using Student's *t*-test: $^{*}P < 0.05$, $^{**}P < 0.01$. **h–k** Confocal microscopy images of dissected germ lines of synchronized young adult of wild type, *mina-1 (ok1521)*, *wago-4(tm2401)*, and *mina-1(ok1521);wago-4(tm2401)* stained for DNA (DAPI, blue) and P granules (antibody K76, red). Arrows highlight the structure and organization of P granules in the different genotypes. Scale bars, 5 µm (germ line section); 1 µm (single germ cell). **l–o** TEM images of wild-type, *mina-1(ok1521)*, *wago-4 (tm2401)*, and *mina-1(ok1521):wago-4(tm2401)* germ cells. Red dotted lines represent the outline of P granules. Scale bar, 1 µm. **p** Higher magnification of area indicated in (**m**, yellow dotted box) shows P granule-associated nuclear pores (arrowheads) in *mina-1* mutant germ cells. Scale bar, 100 nm. **q** P granule average base length in the respective genotypes was analyzed using ImageJ software. Data shown are average ± standard deviation ($n > 50$ germ cells total from three worms for each genotype). P-values were calculated using Student's *t*-test: $^{***}P < 0.001$

The fact that MINA-1 interacts with the WAGO-4 protein and that they both regulate mRNAs post-transcriptionally is intriguing, hinting to a potential co-regulation of target mRNAs. For example, WAGO-4 has recently been shown to coordinate small RNA pathways to direct transgenerational epigenetic inheritance, which suggests that MINA-1 could cooperatively control also how epigenetic information is passed to the next generation [36].

With a broader view, we observed that MINA-1 regulates its own gene product and a cluster of RBPs including the Argonaute proteins WAGO-4 and PPW-2 in gene silencing, FBF proteins in regulating stem cell maintenance, and GLD-1 in promoting meiotic entry, thereby safeguarding proper germ cell differentiation and unwanted cell death. Of note, MINA-1-binding motifs are highly similar to those of two Pumilio proteins that regulate germ cell proliferation, PUF-8 and FBF-1 [23]. This is fascinating, as MINA-1 does not possess any predicted Pumilio family RNA-binding domains, but rather KH RNA-binding domains that usually exhibit different sequence specificity [37].

While the human genome contains eight Argonaute genes [38], *C. elegans* has a larger Argonaute portfolio consisting of 27 genes [10], mostly uncharacterized. Overexpression of Argonaute 1 in neuroblastoma cells has previously been shown to trigger a stronger apoptotic response to UV irradiation [39]. This has functional parallels with the increase of germ cell apoptosis due to WAGO-4 overexpression in *mina-1* mutants. Interestingly, IR-induced apoptosis could not be rescued in *wago-4* mutants, suggesting that another, yet to be determined, putative MINA-1 target is critical for regulating the DNA damage-induced response.

We showed that loss of *mina-1* leads to the enlargement and the disorganization of germline P granules. Min et al. recently showed that the major P granule components PGL-1 and PGL-3 inhibit apoptosis under physiological condition and become crucial targets for inducing higher levels of apoptosis when DNA is damaged [40]. As loss of *mina-1* and loss of *pgl-1* thus share some similar phenotypes, it is possible that the P granule defects observed in *mina-1* contributes to the apoptotic phenotype. Further experiments will be required to test this hypothesis.

Previous research has suggested that WAGO-4 might be a secondary Argonaute in the RNAi machinery [10]. In this report, we additionally identified WAGO-4 as an essential Argonaute for germline-specific RNAi. Furthermore, it was shown that other worm Argonautes like PPW-1, SAGO-1, and SAGO-2 act semi-redundantly and knock-outs cause only mild effects on RNAi [10]. Additionally, we observed that higher amounts of the WAGO-4 proteins cause hypersensitivity of *mina-1* mutants to RNAi. These results are in accordance with previous findings on the overexpression of secondary Argonautes, e.g., SAGO-1, which leads to an increase in RNAi activity [10].

Moreover, we showed that WAGO-4, like several other Argonautes including ALG-3, PRG-1, and CSR-1 [41, 42], is a transient component of P granules and localizes adjacent to P granules in germ cells. The cellular sublocalization of WAGO-4 and MINA-1 support the model postulating that 22G RNAs shuttle between P granules and *Mutator* foci [43]. Due to the functional interaction between MINA-1 and WAGO-4, it is likely that mRNAs shuttling between the P granules and the outer surface of the P granules is managed by these two RBPs. In support of this hypothesis, a recent study postulated that WAGO-4 forms an independent liquid-like condensate, which resides between P granules and Mutator foci [36]. Further research will be needed, to dissect in detail the exact localization of MINA-1 and WAGO-4, and the transport of mRNAs.

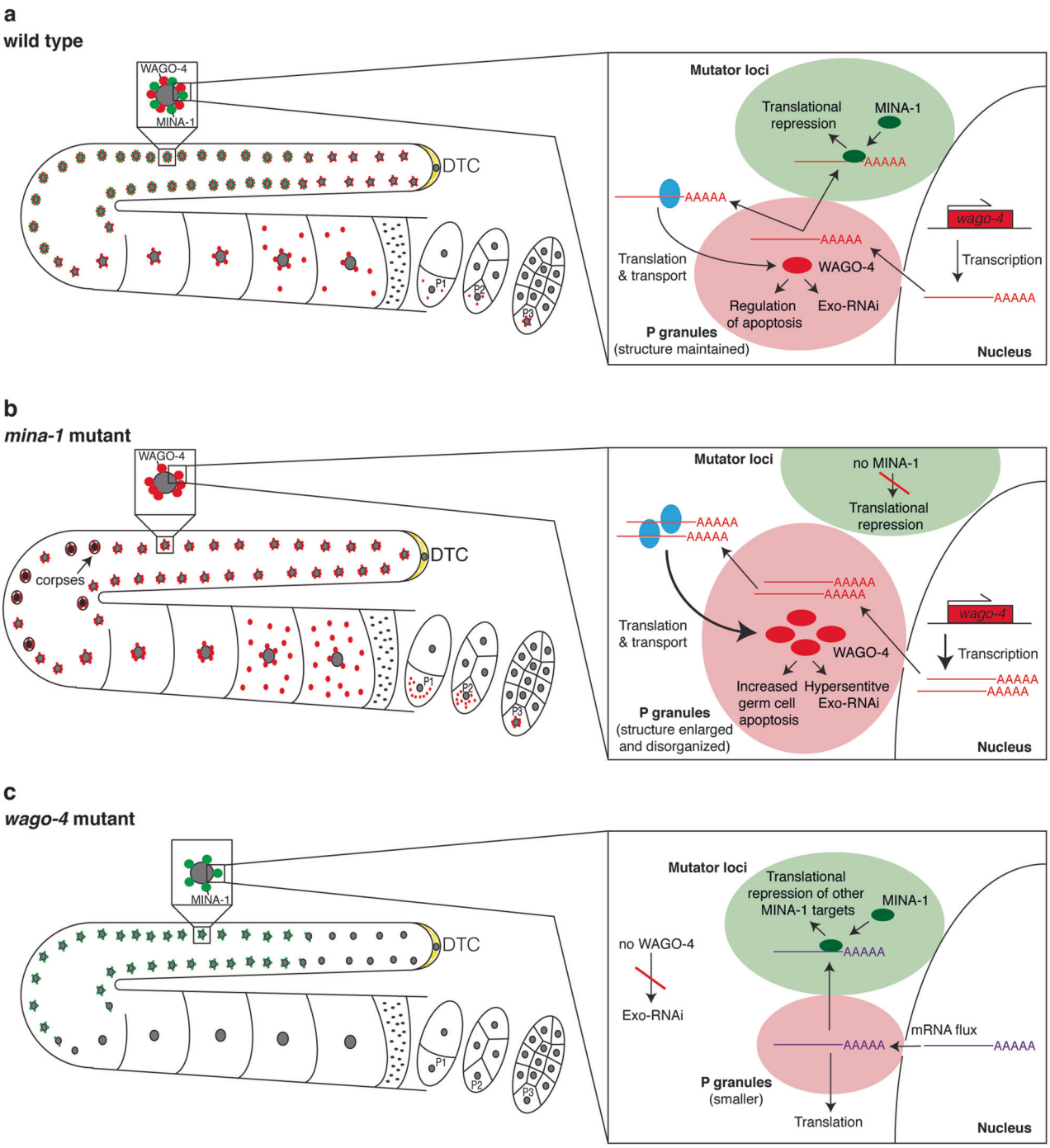

Fig. 6 Model of MINA-1 *wago-4* interaction with its impact on RNAi and apoptosis. **a**-**c** Schematic view of the germ line and first dividing embryos. Magnification of nuclei with surrounding components at nuclear pore complex in the meiotic zone. **a** Wild-type conditions: MINA-1 (green) is expressed in the transition zone until the late pachytene and localizes next to P granules (light red). P granules are organized. MINA-1 partially represses expression of WAGO-4 (green) via binding to 3′-UTR of the *wago-4* transcript and keeps translation at low level. WAGO-4 is expressed through out the germ line and embryos and is always associated with P granules. Germ cell death level is normal. **b** *mina-1* mutant: P granules are enlarged and higher abundant in germ line and embryos. Higher level of *wago-4* transcripts and no repression of WAGO-4 translation lead to higher abundance of WAGO-4 resulting in RNAi hypersensitivity and also increased germ cell death. **c** *wago-4* mutant: no WAGO-4 leads to slightly smaller, but organized P granules. Under these conditions, strains are not sensitive to germline-specific Exo-RNAi

Our findings imply that the previously reported aberrant P granule phenotypes in *mina-1* mutants [44] might be due to an overexpression of WAGO-4. In contrast, WAGO-4 absence does not lead to P granule disorganization or perinuclear localization disruption, which is contradictory to the deletion of the Argonaute CSR-1 [42]. Because of this complex inter-regulatory circuitry of RBPs, targets of the individual RBPs can only be translated when licensed by the community of bound RBPs. This solidifies the emerging concept of the RBP regulon model of "regulators of regulators" [45, 46] (Fig. 6a–c). Further, our findings indicate a highly coordinated RBP network in the germ line. Such a multi-layered RBP coordination is still largely unexplored and we believe that future research will determine many more RBP interactions at the ribonome level, along with their potential to steer biological processes and improve health.

Materials and methods

Strains

All *C. elegans* strains were maintained and raised at 20 °C on nematode growth media (NGM) agar seeded with *Escherichia coli* OP50 (Brenner, 1974). The following mutations and transgenes were used in this study: *mina-1/C41G7.3(ok1521), cep-1(lg12501), ced-9(n1950), rad-5(mn159), wago-4(tm2401), wago-4(tm1019), fbf-1(ok91), gla-3(op216), ced-3(n717), cpb-3(op234), rrf-1(pk1417), mut-7(pk204)*. For SILAC labeling experiment, worms were grown for one generation at 20 °C on NGM plates without peptone (3 g/L NaCl, 20 g/L Bacto-Agar, 5 mg/L cholesterol, 25 mM K_2PO_4, 1 mM $MgSO_4$, 1 mM $CaCl_2$).

DNA damage response assay

Synchronized young adult worms (12 h post L4/adult molt stage) were exposed to X-rays (60 Gy) of UV-C. An Isovolt 160 HS X-ray machine (Rich. Seifert & Co.) or a Stratalinker UV crosslinker, model 1800 (Stratagene) were used. Germline apoptosis was quantified at the indicated time points using differential interference contrast (DIC) microscopy as previously described [15]. For RNAi experiments, synchronized L1 larvae were transferred onto plates seeded with bacteria expressing the respective RNAi clone [47]. Germline apoptosis was quantified as described above, starting from the 12 h post L4/adult molt stage.

Transgenic lines

Low-copy transgenic lines were created by microparticle bombardment as previously described [48], using a Biorad PDS-1000/He Biolistic Delivery System to create transgenic lines of *opIs408(P_{mina-1}::mina-1::gfp::mina-1(3′-UTR) and opIs338(P_{mina-1}::gfp::let-858(3′-UTR)*. All additional lines were created via single copy insertion (MosSCI) [49].

Immunofluorescence staining of extruded germ lines

Animals were placed into 20 µL 0.25 mM levamisole on polylysine-coated slides and cut open close to head and tail using a 25-gauge syringe needle to extract the gonad. With a coverslip set on top of the animals, the slides were transferred into liquid nitrogen for at least 1 min. After incubation in liquid nitrogen, coverslip was immediately popped off, followed by a 10-min incubation in ice-cold methanol. Next, slides were moved in phosphate-buffered saline (PBS) containing 0.1% Tween-20 (PBS-T) for 4 min followed by incubation in PBS containing 1% bovine serum albumin (BSA) for 1 h. Fixed animals were incubated with primary antibody in PBS-T overnight at 4 °C in a humidified chamber. Next day, slides were washed three times in PBS-T for 4 min at room temperature, incubated with secondary antibody for 2 h at 37 °C, and washed three times in PBS-T for 4 min at room temperature. In all, 20 µL of mounting media were added and slides were sealed with nail polish. Antibodies used for staining of extracted germ lines: anti-PGL-1 (1:20,000, gift from S. Strome), anti-Flag M2 (1:5000, mouse, Sigma), anti-Flag (1:1000, rabbit, Sigma), K76 (1:200, mouse, DSHB); anti-GFP (1:1000, Roche), anti-mouse TRITC (1:200, donkey, Jackson IR), and anti-rabbit Alexa Fluor 488 (1:200, rabbit, Jackson IR).

Cloning, expression and purification of MINA-1 (254–334)

The gene encoding residues 254–334 of MINA-1 was amplified by PCR from *C. elegans* complementary DNA (cDNA) using GGAATTCCATATGAAAACATGCGTTG TCGAAAAAATC and CGCGGATCCTTATTTGTCCTG GTGTGATTGCATG as 5′- and 3′-oligonucleotide primers, respectively, and was subcloned into the cell-free expression vector pCFX3 using the *Nde*I and *Bam*HI restriction sites, which results in an N-terminal fusion of the target construct to a tobacco etch virus (TEV) protease-cleavable $(His)_6$-tagged GB1 domain [50]. The "GDDA" variant of MINA-1 (254–334) containing the N276D and R277D mutations was prepared by site-directed mutagenesis (QuikChange II XL, Stratagene) using 5′-GGAAGTAG-GAAAAATATTAGGAGAT GATGCTGCAGTGAAAAAGCATATCG-3′ and 5′-CGA TATGCTTTTTCACTGCAGCATCATCTCCTAATATTT

TTCCTACTTCC-3′ as 5′- and 3′-oligonucleotide primers, respectively. The obtained plasmids were sequence verified and were subsequently amplified for cell-free expression using a plasmid maxi prep kit (Qiagen). The target proteins were subsequently produced in batch mode following a previously described home-made *E. coli*-based cell-free expression system [50]. Uniformly [^{15}N]- and [^{13}C,^{15}N]-labeled protein was obtained in this setup by supplying the cell-free reaction mixture with the respective amino-acid mixture (Spectra Stable Isotopes). Preparative scale expressions were conducted in either 10 or 20 mL reaction volumes and were incubated with gentle agitation for 3 h at 30 °C. Immediately after the expression, the reaction mixture was cleared by centrifugation for 10 min at 5000 × *g* at 4 °C and the obtained supernatant was passed over a 5 mL HisTrap HP column (GE Healthcare) pre-equilibrated with buffer A (50 mM sodium phosphate at pH 7.2, 30 mM imidazole, 500 mM NaCl, 1 mM DTT and 10 µM NaN_3). After washing with 10 column volumes of buffer A, the target protein was eluted in a 100 mL linear gradient of 30–500 mM imidazole in buffer A. The fractions containing the desired protein were identified based on the absorbance at 280 nm and sodium dodecyl sulfate polyacrylamide gel electrophoresis (SDS-PAGE) analysis and were supplied with 0.1 milligram of $(His)_6$-tagged TEV protease [50] per milligram of target protein for an overnight dialysis at 4 °C in a 3.5 kDa MWCO SpectraPor3 dialysis membrane (Spectrum Labs) against 2 L of TEV cleavage buffer (50 mM sodium phosphate at pH 7.2, 100 mM NaCl, 1 mM DTT and 10 µM NaN_3). After TEV cleavage, the solution was passed over a 5 mL HisTrap HP column (GE Healthcare) and the flow-through containing the desired target protein devoid of the $(His)_6$-tagged GB1 domain was collected. The purified protein construct was then dialyzed twice for 12 h at 4 °C in a 3.5 kDa MWCO SpectraPor3 dialysis membrane against 2 L of fresh NMR buffer (20 mM sodium phosphate at pH 5.0, 50 mM NaCl, 2 mM DTT and 0.5 mM EDTA). The dialyzed solution containing the target protein was then concentrated in a 3 kDa MWCO ultracentrifugation device (Millipore) at 4 °C and 3500 × *g* to a final volume of 450 µL and was supplemented with 5% (v/v) D_2O before transfer into a 5TA NMR sample tube (Armar Chemicals).

NMR spectroscopy and structure calculation

All NMR experiments were recorded at 293.15 K on Bruker Avance 500 MHz, 600 MHz, 700 MHz, and 900 MHz spectrometers equipped with CryoProbe™ and triple resonance probes with shielded z-gradient coils. Quadrature detection in the indirect dimensions was achieved by States time-proportional phase incrementation [51]. The water signal was suppressed with spin-lock pulses or WATERGATE [52]. The raw NMR data were processed with TOPSPIN 3.0 (Bruker, Billerica, MA). Proton chemical shifts are referenced to the water resonance and ^{13}C and ^{15}N chemical shifts are indirectly referenced to ^{1}H using the absolute frequency ratios [53]. Backbone resonances were assigned with 3D HNCA [54], 3D HNCACB [54], and 3D CBCA(CO)NH [55] experiments, whereas side-chain resonances were assigned (BMRB ID 34220) using the 3D (H)CC(CO)NH [56], 3D H(CC)(CO)NH [56], and 3D [^{15}N,^{1}H]-HSQC-TOCSY [57] experiments based on an NMR sample containing 1 mM of uniformly [^{13}C,^{15}N]-labeled MINA-1 (254–334) in NMR buffer. NOE-based distance constraints for the structure calculation were obtained from 3D ^{15}N-resolved [^{1}H, ^{1}H]-NOESY, 3D aliphatic ^{13}C-resolved [^{1}H,^{1}H]-NOESY and 3D aromatic ^{13}C-resolved [^{1}H,^{1}H]-NOESY spectra [58, 59], which were recorded with a mixing time of 60 ms. The protocol for calculation of the solution structure of MINA-1 (254–334) was based on the ATNOS [60] procedure for automated peak picking and used the list of picked peaks from cycle two in combination with the chemical shift list from the sequence-specific resonance assignment and the 3D NOESY spectra as input for automated NOESY assignment and structure calculation in the program CYANA [60, 61]. The final structure calculation in cycle 7 included only unambiguously assigned distance constraints based on the calculated 3D structure from cycle 6. The 20 conformers with the lowest residual target function obtained from cycle 7 were then energy minimized in implicit water using the program AMBER12 [62]. The RNA for the NMR titration experiments was purchased from GE Dharmacon and was deprotected following the manufacturers protocol and was subsequently lyophilized and dissolved in NMR buffer. For spectral analysis, the program CARA (www.nmr.ch) was used . The programs MOLMOL [63] and PyMOL (Schrödinger, LLC) were used for visualization of the protein structures.

Stable isotope labeling by amino acids in nematodes (SILAC)

The *E. coli* strains were labeled with heavy and light isotopes as described previously [64]. Isotopically labeled samples of wild-type, *mina-1(ok1521) C. elegans* strains were prepared by feeding worms with heavy and light labeled bacteria for one generation. Bleach-synchronized L1 worms that hatched on unseeded plates overnight were transferred to the plates with light (40,000 worms) and heavy labeled (120,000 worms) bacteria, respectively (20,000 worms/plate), and collected at the young adult stage for subsequent protein and RNA isolation (68 h post-transfer). Two biological replicates were grown for the comparison of *mina-1* with wild type.

Protein extraction and orbitap mass spectrometry

Proteins were extracted from worms using 50 mM Tris/HCl (pH 8.3), 5 mM EDTA, 8 M urea buffer and glass beads [65]. The protein concentrations of the purified extracts were determined by the Bradford assay (using Bradford reagent, Sigma-Aldrich). For the SILAC experiments, two heavy standards were prepared. In all, 100 µg of protein extract labeled with heavy lysine ($^{15}N_{2,}{}^{13}C_6$-L-lysine) and arginine ($^{15}N_{4,}{}^{13}C_6$-L-arginine) from each wild-type, *mina-1, gla-3*, and *cpb-3* strains was mixed and used for the mina-1/wild type comparison. For *mina-1* sample, 100 µg (*wago-4* 150 µg) of light labeled *C. elegans* protein extracts were mixed with 100 µg (*wago-4* 150 µg) of heavy labeled internal standard proteome, followed by precipitation with six volumes of ice-cold acetone (only *mina-1* samples). Protein extraction, precipitation, digestion, HILIC fractionation, Orbitrap mass spectrometry measurements, and statistical analysis were performed as described previously [64, 66].

RNA isolation

RNA was isolated by TRIzol (Life Technologies) according to the manufacturer's protocol and additionally purified by a solution of acidic phenol: chloroform (5:1) pH 4.5 (Ambion) followed by a second chloroform extraction to obtain high-grade RNA for sequencing. Finally, DNA traces were degraded by DNAse I (Ambion).

Transcriptome sequencing and analysis

RNA was isolated from three biological replicates of wild-type and *mina-1* mutant strains and the transcriptome was sequenced by GATC Biotech (Konstanz, Germany). The differential expression analysis was done by the count-based approach, as previously described [66]. Version numbers of various software tools used are as follows. For wild type and *mina-1* samples: ShortRead (version 1.22.0) [67], *C. elegans* reference genome WBcel235 (release-74), TopHat (version 2.0.10) [68], HTSeq (version 0.5.4p5) [69], and edgeR (version 3.4.2) [70].

HITS-CLIP

C. elegans animals from a transgene expressing MINA-1::GFP ($P_{mina\text{-}1}$*::mina-1(genomic)::GFP::mina-1 3′-UTR*) were bleached and their progeny grown on plates for 68 h at 20 °C until they reached the young adult stage. Three biological replicates were harvested and irradiated with UV-B (3 kJ/m^2) as described [71]. Around 200,000 worms were collected for one CLIP experiment. Irradiated and washed worm pellets were lysed by sonication in RIPA buffer (25 mM HEPES-K at pH 7.5, 100 mM KCl, 1% [v/v] NP-40, 0.25% [v/v] sodium deoxycholate, 0.1% [v/v] SDS, 0.5 mM DTT, protease inhibitor cocktail, Roche). Cleared lysates were digested with RNase T1 (Fermentas) (final concentration 1 unit/µL) for 15 min at 22 °C. Subsequently, MINA-1::GFP fusion proteins were immunoprecipitated with GFP-trap beads (ChromoTek) for 1 h at 4 °C. In all, 150 µL of beads were used for one experiment. RNA labeling and cDNA library preparation were performed according to the PAR-CLIP protocol [72]. cDNA libraries were sequenced with Genome Analyzer IIx (Illumina). Mapping and annotation were performed as described [73] using *C. elegans* genome build ce6. CLIP-Seq data normalization was performed as described [73].

Protein–protein immunoprecipitation

Worms expressing MINA-1::GFP were bleached, synchronized, and grown for 68 h at 20 °C before harvesting at the young adult stage. Young adult animals expressing proteins HUS-1::GFP [74], CED-4::GFP [75], and LET-99::GFP [13] reported to be expressed in the *C. elegans* germ line were used as negative controls. As transgenic worms expressing HUS-1::GFP grows slower they were collected 77 h post-bleaching. Around 400 µL of worm pellets were lysed in co-immunoprecipitation (co-IP) buffer (100 mM Tris/HCl pH 8.0, 150 mM NaCl, 1 mM DTT, 1 mM EDTA; 0.7% IGEPAL, Roche Protease Inhibitor tablet) for 20 min on a rotating wheel at 4 °C. Lysates were frozen in liquid N_2 and pulverized the lysate with a swing-mill (3 × 2 min at 30 Hz). Immunoprecipitation and washing steps were performed as instructed by the manufacturer, with a modification of the wash buffer (100 mM Tris/HCl pH 8.0, 150 mM NaCl, 1 mM EDTA). Beads were eluted with 4× lithium dodecyl sulfate (LDS) buffer and reducing agent (Invitrogen) for 10 min at 95 °C. Co-immunoprecipitated proteins were separated on an (4–12%) SDS-PAGE gel (Invitrogen). Three biological replicates of the MINA-1::GFP IP and CED-4::GFP IP were performed, four of HUS-1::GFP IP and two of LET-99:GFP IP.

Microarray analysis of MINA-1 IP vs. HUS-1 IP

MINA-1::GFP and HUS-1::GFP [74] expressing animals were grown and lysed as described for protein–protein interaction experiments with the difference that the co-IP buffer was supplemented with 100 units/mL RNase OUT (Life Technologies). Washing was performed with wash buffer (100 mM Tris-HCl pH: 8.0, 150 mM NaCl, 1 mM EDTA) and proteins were eluted for 30 min at 55 °C with wash buffer supplemented with 1% SDS and 1.2 mg/mL Proteinase K [76]. RNA was purified from the supernatants by phenol:chloroform extraction and precipitated

with ethanol. In all, 100 ng of co-immunoprecipitated RNA was used for cDNA preparation and amplification using Amino Allyl Message Amp II aRNA Amplification Kit (Thermo Fisher). MINA-1 and HUS-1 cDNAs were labeled with Cy3 and Cy5 fluorescent dyes, respectively. The Cy3- and Cy5-labeled cDNA samples were mixed and competitively hybridized to the whole-genome *C. elegans* DNA microarrays, produced by the Genome Sequencing Center at Washington University in St. Louis. Microarrays were scanned with an Axon Instruments Scanner 4200A (Molecular Devices) and data were processed as described previously [77]. One experiment comparing differential IP enrichment of MINA-1 to HUS-1 was performed.

Protein identification with Orbitrap mass spectrometry

Each of the gel lanes was cut into four pieces. Each piece was washed twice with 100 µL of 100 mM NH_4HCO_3/50% acetonitrile and once with 50 µL acetonitrile. Proteins were digested with 10 µL trypsin (10 ng/µL in 10 mM Tris/2 mM $CaCl_2$, pH 8.2) in 50 µL buffer A (10 mM Tris/2 mM $CaCl_2$, pH 8.2) were added, followed by heating in a microwave oven for 30 min at 60 °C. Peptides were extracted with 150 µL 0.1% TFA/50% acetonitrile. All supernatants were combined and vacuum dried. Peptides were dissolved in 20 µL 0.1% trifluoroacetic acid (TFA), desalted on ZipTip C18, eluted in 20 µL 0.1% TFA/60% acetonitrile, dried, dissolved in 15 µL 0.2% formic acid/3% acetonitrile and transferred to autosampler vials for LC/MS/MS. In all, 10 µL of the peptide was injected into the Orbitrap mass spectrometer. Database searches were performed by using the Mascot (*C. elegans* database) search program.

Qualitative evaluation of GFP signal of *fbf-1 3′-UTR* reporter line in *mina-1* mutant and after *mina-1* RNAi

To analyze the inhibition of *fbf-1* expression in mina-1 background, adult worms of JH2270 *fbf-1* reporter line (P_{pie-1}*::gfp::h2b::fbf-1(3′-UTR))* [29] and *mina-1;* P_{pie-1}*:: gfp::h2b::fbf-1(3′-UTR)* were bleached and synchronized. L1 larvae were transferred into the plates seeded with op50 separately. GFP fluorescence intensities were detected through Leica microscope 24 h post L4 larvae/adult molt stage. For RNAi, adult worms of JH2270 *fbf-1* reporter line (P_{pie-1}*::gfp::h2b::fbf-1(3′-UTR))* were bleached and synchronized L1 larvae were transferred into the plates seeded with RNAi empty vector and *mina-1(RNAi)* separately. GFP fluorescence intensities were detected through Leica microscope 24 h post L4 larvae/adult molt stage.

Immunostaining of isolated embryos

After bleaching, resuspended embryos were transferred on poly-lysine slides. Once the embryos were settled on the slide, they were fixed with 150 µL 5% formaldehyde and subsequently covered with a 22 × 22 mm cover slip. After fixation in a humid chamber for 30 min, slides were immerged in liquid N_2 and incubated for 20 min. The cover slip popped off immediately and slides were placed in 100% methanol for 4 min. Samples were blocked with 150 µL 1% BSA for 30 min and stained with 150 µL first antibody in 1% BSA for 1 h. After washing three times in TBS-T for 4 min, slides were stained with 150 µL secondary antibody for 1 min. DNA was stained with 1:5000 Hoechst staining dilution for 1 min. In the last step, slides were mounted with 20 µL Mowiol, covered with a 22 × 22 mm cover slip, and sealed with nail polish. All steps were carried out at room temperature (RT) (adapted from [78]). Antibodies used to stain embryos: anti-Flag M2 (1:5000, mouse, Sigma), anti-Flag (1:1000, rabbit, Sigma), K76 (1:200, mouse, DSHB); anti-GFP (1:1′000, Roche), anti-mouse TRITC (1:200, donkey, Jackson IR), and anti-rabbit Alexa Fluor 488 (1:200, rabbit, Jackson IR).

TEM

Wild-type, *mina-1(ok1521), mina-1(ok1521)* animals grown on *E. coli* on NGM agar plates were high-pressure frozen with an EM HPM100 (Leica Microsystems, Vienna, Austria) high-pressure freezing machine in two ways. (i) Five to ten worms were picked from an agar plate and transferred to a droplet of M9 medium in the 100 µm cavity of a 3 mm aluminum specimen carrier. M9 was drawn off with a filter paper, the sandwich was completed with a flat 3 mm aluminum specimen carrier wetted with 1-hexadecene, and frozen immediately. (ii) Animals were rinsed off an agar plate using M9 medium and transferred into a 1 mL reaction tube in which worms sedimented after a minute. Supernatant was discarded and worms were drawn into cellulose capillary tubes. Subsequently, the cellulose capillary tubes were cut into pieces of 3–4 mm length in 1-hexadecene, transferred into the 150 µm cavity of a 6 mm aluminum specimen carrier, sandwiched with a flat 6 mm aluminum specimen carrier wetted with 1-hexadecene, and frozen immediately. Frozen specimens were freeze substituted in anhydrous acetone containing 1% OsO_4 in a Leica EM AFS2 freeze substitution unit (Leica Microsystems) and kept successively at –90 °C for 8 h, –60 °C for 4 h, –30 °C for 3 h, and 0 °C for 1 h using temperature transition gradients of 30 °C/h. Specimens were rinsed twice with anhydrous acetone, incubated in 1% uranyl acetate in anhydrous acetone for 1 h at 4 °C, rinsed twice with anhydrous acetone, gradually embedded in Epon/Araldite

(Sigma-Aldrich, Buchs, Switzerland), 66% resin in anhydrous acetone for 3 h at 4 °C, followed by 100% resin 1 h at RT, and polymerized at 60 °C for 20 h. Thin sections of 70 nm were stained with 2% aqueous uranyl acetate and Reynolds lead citrate and imaged in a Philips CM 100 transmission electron microscope (FEI, Eindhoven, The Netherlands) using a Gatan Orius 1000 CCD camera and digital micrograph acquisition software (Gatan GmbH, Munich, Germany).

RNAi experiment

RNAi experiments were performed as described previously [47]. Apoptotic corpses were scored as previously described [79]. For RNAi resistance experiments, *mut-7(pk204)* and *rrf-1(pk1417)* mutant animals were used as control for germline and soma-specific RNAi resistance, respectively.

Primers

Cloning of *Pmina-1::mina-1::gfp::mina-1(3′-UTR)* construct used for opIs408:

mina-1 promoter and gene:

5′-TATACCTGCAGGCATTGTGCCTTTCACATCC TCATC-3′;

5′-TTTTGGCCGGCCATCAGACGGGGAAAGTTT ACGTGGT-3′.

mina-1 3′-UTR:

5′-ATATTTAATTAAGTAAACTTTCCCCGTCTGAT TAATA-3′;

5-TATAACTAGTCTGTAAGAAAAAATTGGTTTG CGAA-3′.

wago-4 promotor:

5′-TGTTTCTCGTTGCTTGTCCTGATTGTTCC-3′;

5′-CCTTCTCGATTTTGTAACTATTACCTG-3′.

wago-4 gene:

5′-ATGCCAGCTCTTCCTCCAGTCTACACG-3′;

5′-TGCGTTGACACGACGACCCGTGAGATC-3′.

wago-4 3′-UTR:

5′-TCACTTTCAACAAGGCAAACTTTGTTTC-3′;

5′-AATGCTCTTCACAAATTCACGAACCTG-3′.

Acknowledgements We acknowledge financial support from Sinergia grants of the Swiss National Science Foundation (grant numbers 141942 and 143932) and members of our laboratories for helpful discussion. AS was supported by the People Programme (Marie Curie Actions) of the European Union's Seventh Framework Programme FP7 under REA grant agreement no. 629861.

Author contributions AS, DS, LD, MK, and EM performed the in silico analyses, wet lab experiments, and wrote the manuscript. IK and XZ helped performing wet lab experiments and contributed to general discussions and writing the manuscript. KS analyzed the RNA-seq and SILAC data and contributed to figures, general discussions, and comments for the manuscript. AB, JI, and SK contributed to the HITS-CLIP experiments and to the corresponding in silico analyses, discussed and interpreted the results, and provided detailed comments to the manuscript. YW helped performing the SILAC experiment, contributed to general discussions. A Kanitz and AMM-G contributed to perform and analyze RIP-chip experiments, general discussion and manuscript writing and revision. A Kaech helped performing TEM experiments, contributed to general discussions and added comments to the manuscript. NM contributed to the RNA sequencing experiments and to general discussions and writing the manuscript. APG added general advice on the study, provided resources for RIP-chip experiments, and contributed to the writing of the manuscript. MZ supervised and provided resources for HITS-CLIP experiments, discussed and interpreted the results, and revised the manuscript. RA, JH discussed and interpreted the results, and revised the manuscript. FH-TA contributed to general discussion, provided resources for the structural analyses, revised the manuscript. MOH supervised and guide the entire project, provided resources for all the in vivo experiments, helped in interpreting the results and writing the manuscript.

Data availability The atomic coordinates and the NMR assignments have been deposited in the Protein Data Bank under accession code 6FBL and in the Biological Magnetic Resonance Bank under accession code 34220, respectively. CLIP, microarray, and transcriptomics data are available in the ArrayExpress database at EMBL-EBI (http://www.ebi.ac.uk/) under accession number E-MTAB-7420, E-MTAB-7415, and E-MTAB-7389, respectively. SILAC data have been deposited to the ProteomeXchange Consortium (http://proteomecentral.proteomexchange.org) via the PRIDE partner repository with the dataset identifier (PXD011625).

Compliance with ethical standards

Conflict of interest The authors declare that they have no conflict of interest.

Publisher's note: Springer Nature remains neutral with regard to jurisdictional claims in published maps and institutional affiliations.

References

1. Glisovic T, Bachorik JL, Yong J, Dreyfuss G. RNA-binding proteins and post-transcriptional gene regulation. FEBS Lett. 2008;582:1977–86.
2. Keene JD. RNA regulons: coordination of post-transcriptional events. Nat Rev Genet. 2007;8:533–43.
3. Moore MJ. From birth to death: the complex lives of eukaryotic mRNAs. Science. 2005;309:1514–8.
4. Lukong KE, Chang K-W, Khandjian EW, Richard S. RNA-binding proteins in human genetic disease. Trends Genet. 2008;24:416–25.
5. Kimble J, Crittenden SL. Controls of germline stem cells, entry into meiosis, and the sperm/oocyte decision in Caenorhabditis elegans. Annu Rev Cell Dev Biol. 2007;23:405–33.
6. Wright JE, Gaidatzis D, Senften M, Farley BM, Westhof E, Ryder SP, et al. A quantitative RNA code for mRNA target selection by the germline fate determinant GLD-1. EMBO J. 2011;30:533–45.
7. Ciosk R, DePalma M, Priess JR. Translational regulators maintain totipotency in the *Caenorhabditis elegans* germline. Science. 2006;311:851–3.
8. Subasic D, Stoeger T, Eisenring S, Matia-González AM, Imig J, Zheng X, et al. Post-transcriptional control of executioner caspases by RNA-binding proteins. Genes Dev. 2016;30:2213–25.
9. Bukhari SIA, Vasquez-Rifo A, Gagné D, Paquet ER, Zetka M, Robert C, et al. The microRNA pathway controls germ cell

proliferation and differentiation in *C. elegans*. Cell Res. 2012;22:1034–45.
10. Yigit E, Batista PJ, Bei Y, Pang KM, Chen C-CG, Tolia NH, et al. Analysis of the *C. elegans* Argonaute family reveals that distinct Argonautes act sequentially during RNAi. Cell. 2006;127:747–57.
11. Sheth U, Pitt J, Dennis S, Priess JR. Perinuclear P granules are the principal sites of mRNA export in adult *C. elegans* germ cells. Development. 2010;137:1305–14.
12. Currie JR, Brown WT. KH domain-containing proteins of yeast: absence of a fragile X gene homologue. Am J Med Genet. 1999;84:272–6.
13. Sendoel A, Maida S, Zheng X, Teo Y, Stergiou L, Rossi C-A, et al. DEPDC1/LET-99 participates in an evolutionarily conserved pathway for anti-tubulin drug-induced apoptosis. Nat Cell Biol. 2014;16:812–20.
14. Valverde R, Edwards L, Regan L. Structure and function of KH domains. FEBS J. 2008;275:2712–26.
15. Gumienny TL, Lambie E, Hartwieg E, Horvitz HR, Hengartner MO. Genetic control of programmed cell death in the *Caenorhabditis elegans* hermaphrodite germline. Development. 1999;126:1011–22.
16. Aballay A, Ausubel FM. Programmed cell death mediated by ced-3 and ced-4 protects *Caenorhabditis elegans* from Salmonella typhimurium-mediated killing. Proc Natl Acad Sci USA. 2001;98:2735–9.
17. Parrish J, Metters H, Chen L, Xue D. Demonstration of the in vivo interaction of key cell death regulators by structure-based design of second-site suppressors. Proc Natl Acad Sci USA. 2000;97:11916–21.
18. Nicastro G, Taylor IA, Ramos A. KH-RNA interactions: back in the groove. Curr Opin Struct Biol. 2015;30:63–70.
19. Hollingworth D, Candel AM, Nicastro G, Martin SR, Briata P, Gherzi R, et al. KH domains with impaired nucleic acid binding as a tool for functional analysis. Nucleic Acids Res. 2012; 40:6873–86.
20. Kishore S, Jaskiewicz L, Burger L, Hausser J, Khorshid M, Zavolan M. A quantitative analysis of CLIP methods for identifying binding sites of RNA-binding proteins. Nat Methods. 2011;8:559–64.
21. Licatalosi DD, Mele A, Fak JJ, Ule J, Kayikci M, Chi SW, et al. HITS-CLIP yields genome-wide insights into brain alternative RNA processing. Nature. 2008;456:464–9.
22. Bailey TL, Williams N, Misleh C, Li WW. MEME: discovering and analyzing DNA and protein sequence motifs. Nucleic Acids Res. 2006;34:W369–73.
23. Opperman L, Hook B, DeFino M, Bernstein DS, Wickens M. A single spacer nucleotide determines the specificities of two mRNA regulatory proteins. Nat Struct Mol Biol. 2005;12:945–51.
24. Kershner AM, Kimble J. Genome-wide analysis of mRNA targets for *Caenorhabditis elegans* FBF, a conserved stem cell regulator. Proc Natl Acad Sci USA. 2010;107:3936–41.
25. Mukherjee N, Corcoran DL, Nusbaum JD, Reid DW, Georgiev S, Hafner M, et al. Integrative regulatory mapping indicates that the RNA-binding protein HuR couples pre-mRNA processing and mRNA stability. Mol Cell. 2011;43:327–39.
26. Teplova M, Malinina L, Darnell JC, Song J, Lu M, Abagyan R, et al. Protein-RNA and protein-protein recognition by dual KH1/2 domains of the neuronal splicing factor Nova-1. Structure. 2011;19:930–44.
27. Daubner GM, Brümmer A, Tocchini C, Gerhardy S, Ciosk R, Zavolan M, et al. Structural and functional implications of the QUA2 domain on RNA recognition by GLD-1. Nucleic Acids Res. 2014;42:8092–105.
28. Huang DW, Sherman BT, Lempicki RA. Systematic and integrative analysis of large gene lists using DAVID bioinformatics resources. Nat Protoc. 2009;4:44–57.
29. Merritt C, Rasoloson D, Ko D, Seydoux G. 3' UTRs are the primary regulators of gene expression in the C. elegans germline. Curr Biol. 2008;18:1476–82.
30. Brümmer A, Kishore S, Subasic D, Hengartner M, Zavolan M. Modeling the binding specificity of the RNA-binding protein GLD-1 suggests a function of coding region-located sites in translational repression. RNA. 2013;19:1317–26.
31. Jungkamp A-C, Stoeckius M, Mecenas D, Grün D, Mastrobuoni G, Kempa S, et al. In vivo and transcriptome-wide identification of RNA binding protein target sites. Mol Cell. 2011;44:828–40.
32. Crittenden SL, Bernstein DS, Bachorik JL, Thompson BE, Gallegos M, Petcherski AG, et al. A conserved RNA-binding protein controls germline stem cells in *Caenorhabditis elegans*. Nature. 2002;417:660–3.
33. Imig J, Kanitz A, Gerber AP. RNA regulons and the RNA-protein interaction network. Biomol Concepts. 2012;3:403–14.
34. Mittal N, Scherrer T, Gerber AP, Janga SC. Interplay between posttranscriptional and posttranslational interactions of RNA-binding proteins. J Mol Biol. 2011;409:466–79.
35. Tabara H, Sarkissian M, Kelly WG, Fleenor J, Grishok A, Timmons L, et al. The rde-1 gene, RNA interference, and transposon silencing in *C. elegans*. Cell. 1999;99:123–32.
36. Wan G, Fields BD, Spracklin G, Shukla A, Phillips CM, Kennedy S. Spatiotemporal regulation of liquid-like condensates in epigenetic inheritance. Nature. 2018;557:679–83.
37. Ray D, Kazan H, Cook KB, Weirauch MT, Najafabadi HS, Li X, et al. A compendium of RNA-binding motifs for decoding gene regulation. Nature. 2013;499:172–7.
38. Hutvagner G, Simard MJ. Argonaute proteins: key players in RNA silencing. Nat Rev Mol Cell Biol. 2008;9:22–32.
39. Parisi C, Giorgi C, Batassa EM, Braccini L, Maresca G, D'agnano I, et al. Ago1 and Ago2 differentially affect cell proliferation, motility and apoptosis when overexpressed in SH-SY5Y neuroblastoma cells. FEBS Lett. 2011;585:2965–71.
40. min H, Shim YH, Kawasaki I. Loss of PGL-1 and PGL-3, members of a family of constitutive germ-granule components, promotes germline apoptosis in *C. elegans*. J Cell Sci. 2016;129:341–53.
41. Batista PJ, Ruby JG, Claycomb JM, Chiang R, Fahlgren N, Kasschau KD, et al. PRG-1 and 21U-RNAs interact to form the piRNA complex required for fertility in *C. elegans*. Mol Cell. 2008;31:67–78.
42. Claycomb JM, Batista PJ, Pang KM, Gu W, Vasale JJ, van Wolfswinkel JC, et al. The Argonaute CSR-1 and its 22G-RNA cofactors are required for holocentric chromosome segregation. Cell. 2009;139:123–34.
43. Youngman EM, Claycomb JM. From early lessons to new frontiers: the worm as a treasure trove of small RNA biology. Front Genet. 2014;5:416.
44. Updike DL, Strome S. A genomewide RNAi screen for genes that affect the stability, distribution and function of P granules in *Caenorhabditis elegans*. Genetics. 2009;183:1397–419.
45. Mansfield KD, Keene JD. The ribonome: a dominant force in co-ordinating gene expression. Biol Cell. 2009;101:169–81.
46. Pullmann R, Kim HH, Abdelmohsen K, Lal A, Martindale JL, Yang X, et al. Analysis of turnover and translation regulatory RNA-binding protein expression through binding to cognate mRNAs. Mol Cell Biol. 2007;27:6265–78.
47. Kamath RS, Fraser AG, Dong Y, Poulin G, Durbin R, Gotta M, et al. Systematic functional analysis of the *Caenorhabditis elegans* genome using RNAi. Nature. 2003;421:231–7.
48. Praitis V, Casey E, Collar D, Austin J. Creation of low-copy integrated transgenic lines in *Caenorhabditis elegans*. Genetics. 2001;157:1217–26.
49. Frøkjaer-Jensen C, Davis MW, Hopkins CE, Newman BJ, Thummel JM, Olesen S-P, et al. Single-copy insertion of transgenes in *Caenorhabditis elegans*. Nat Genet. 2008;40:1375–83.

50. Michel E, Wüthrich K. High-yield *Escherichia coli*-based cell-free expression of human proteins. J Biomol NMR. 2012;53:43–51.
51. Marion D, Wüthrich K. Application of phase sensitive two-dimensional correlated spectroscopy (COSY) for measurements of 1H-1H spin-spin coupling constants in proteins. Biochem Biophys Res Commun. 1983;113:967–74.
52. Piotto M, Saudek V, Sklenár V. Gradient-tailored excitation for single-quantum NMR spectroscopy of aqueous solutions. J Biomol NMR. 1992;2:661–5.
53. Wishart DS, Bigam CG, Yao J, Abildgaard F, Dyson HJ, Oldfield E, et al. 1H, 13C and 15N chemical shift referencing in biomolecular NMR. J Biomol NMR. 1995;6:135–40.
54. Kay LE, Ikura M, Tschudin R, Bax A. Three-dimensional triple-resonance NMR spectroscopy of isotopically enriched proteins. 1990. J Magn Reson. 2011;213:423–41.
55. Grzesiek S, Bax A. Amino acid type determination in the sequential assignment procedure of uniformly 13C/15N-enriched proteins. J Biomol NMR. 1993;3:185–204.
56. Montelione GT, Lyons BA, Emerson SD, Tashiro M. An efficient triple resonance experiment using carbon-13 isotropic mixing for determining sequence-specific resonance assignments of isotopically-enriched proteins. J Am Chem Soc. 1992;114:10974–5.
57. Marion D, Driscoll PC, Kay LE, Wingfield PT, Bax A, Gronenborn AM, et al. Overcoming the overlap problem in the assignment of 1H NMR spectra of larger proteins by use of three-dimensional heteronuclear 1H-15N Hartmann-Hahn-multiple quantum coherence and nuclear Overhauser-multiple quantum coherence spectroscopy: application to interleukin 1 beta. Biochemistry. 1989;28:6150–6.
58. Ikura M, Kay LE, Tschudin R, Bax A. Three-dimensional NOESY-HMQC spectroscopy of a 13C-labeled protein. J Magn Reson. 1990;86:204–9.
59. Talluri S, Wagner G. An optimized 3D NOESY-HSQC. J Magn Reson B. 1996;112:200–5.
60. Herrmann T, Güntert P, Wüthrich K. Protein NMR structure determination with automated NOE assignment using the new software CANDID and the torsion angle dynamics algorithm DYANA. J Mol Biol. 2002;319:209–27.
61. Güntert P. Automated NMR structure calculation with CYANA. Methods Mol Biol. 2004;278:353–78.
62. Case DA, Darden TA, Cheatham TE, Simmerling CL, Wang J, Duke RE, et al. AMBER 12. San Francisco: University of California; 2012. p. 1–350.
63. Koradi R, Billeter M, Wüthrich K. MOLMOL: a program for display and analysis of macromolecular structures. J Mol Graph. 1996;14:51–5. 29–32
64. Subasic D, Brümmer A, Wu Y, Pinto SM, Imig J, Keller M, et al. Cooperative target mRNA destabilization and translation inhibition by miR-58 microRNA family in *C. elegans*. Genome Res. 2015;25:1680–91.
65. Schrimpf SP, Weiss M, Reiter L, Ahrens CH, Jovanovic M, Malmström J, et al. Comparative functional analysis of the *Caenorhabditis elegans* and *Drosophila melanogaster* proteomes. PLoS Biol. 2009;7:e48.
66. Singh KD, Zheng X, Milstein S, Keller M, Roschitzki B, Grossmann J, et al. Differential regulation of germ line apoptosis and germ cell differentiation by CPEB family members in *C. elegans*. PLoS ONE. 2017;12:e0182270.
67. Morgan M, Anders S, Lawrence M, Aboyoun P, Pagès H, Gentleman R. ShortRead: a bioconductor package for input, quality assessment and exploration of high-throughput sequence data. Bioinformatics. 2009;25:2607–8.
68. Trapnell C, Pachter L, Salzberg SL. TopHat: discovering splice junctions with RNA-Seq. Bioinformatics. 2009;25:1105–11.
69. Anders S, Pyl PT, Huber W. HTSeq–a Python framework to work with high-throughput sequencing data. Bioinformatics. 2015;31:166–9.
70. Robinson MD, McCarthy DJ, Smyth GK. edgeR: a Bioconductor package for differential expression analysis of digital gene expression data. Bioinformatics. 2010;26:139–40.
71. Zisoulis DG, Lovci MT, Wilbert ML, Hutt KR, Liang TY, Pasquinelli AE, et al. Comprehensive discovery of endogenous Argonaute binding sites in *Caenorhabditis elegans*. Nat Struct Mol Biol. 2010;17:173–9.
72. Hafner M, Landthaler M, Burger L, Khorshid M, Hausser J, Berninger P, et al. PAR-CliP–a method to identify transcriptome-wide the binding sites of RNA binding proteins. J Vis Exp. 2010;41:e2034.
73. Khorshid M, Rodak C, Zavolan M. CLIPZ: a database and analysis environment for experimentally determined binding sites of RNA-binding proteins. Nucleic Acids Res. 2011;39:D245–52.
74. Hofmann ER, Milstein S, Boulton SJ, Ye M, Hofmann JJ, Stergiou L, et al. *Caenorhabditis elegans* HUS-1 is a DNA damage checkpoint protein required for genome stability and EGL-1-mediated apoptosis. Curr Biol. 2002;12:1908–18.
75. Zermati Y, Mouhamad S, Stergiou L, Besse B, Galluzzi L, Boehrer S, et al. Nonapoptotic role for Apaf-1 in the DNA damage checkpoint. Mol Cell. 2007;28:624–37.
76. Jain A, Liu R, Ramani B, Arauz E, Ishitsuka Y, Ragunathan K, et al. Probing cellular protein complexes using single-molecule pull-down. Nature. 2011;473:484–8.
77. Jovanovic M, Reiter L, Clark A, Weiss M, Picotti P, Rehrauer H, et al. RIP-chip-SRM–a new combinatorial large-scale approach identifies a set of translationally regulated bantam/miR-58 targets in *C. elegans*. Genome Res. 2012;22:1360–71.
78. Bowerman B, Eaton BA, Priess JR. skn-1, a maternally expressed gene required to specify the fate of ventral blastomeres in the early *C. elegans* embryo. Cell. 1992;68:1061–75.
79. Lettre G, Hengartner MO. Developmental apoptosis in *C. elegans*: a complex CEDnario. Nat Rev Mol Cell Biol. 2006;7:97–108.

Affiliations

Ataman Sendoel[1] · Deni Subasic[1,2] · Luca Ducoli[1,2,3] · Martin Keller[1,2] · Erich Michel[4,11,11] · Ines Kohler[1] · Kapil Dev Singh[1,2,12,12] · Xue Zheng[1] · Anneke Brümmer[5] · Jochen Imig[3,5,13,14,13,14] · Shivendra Kishore[5] · Yibo Wu[6,7] · Alexander Kanitz[5] · Andres Kaech[8] · Nitish Mittal[5] · Ana M. Matia-González[9] · André P. Gerber[9] · Mihaela Zavolan[5] · Ruedi Aebersold[6,10] · Jonathan Hall[3] · Frédéric H.-T. Allain[4] · Michael O. Hengartner[1,10]

[1] Institute of Molecular Life Sciences, University of Zurich, Winterthurerstrasse 190, 8057 Zurich, Switzerland

[2] PhD Program in Molecular Life Sciences, University of Zurich and ETH Zurich, Winterthurerstrasse 190, 8057 Zurich, Switzerland

[3] Institute of Pharmaceutical Sciences, ETH Zurich, Wolfgang-Pauli-Strasse 10, 8093 Zürich, Switzerland

[4] Institute of Molecular Biology and Biophysics, ETH Zurich, Auguste-Piccard-Hof 1, 8093 Zurich, Switzerland

[5] Biozentrum, University of Basel, Klingelbergstrasse 50/70, 4056 Basel, Switzerland

[6] Institute of Molecular Systems Biology, ETH Zurich, Auguste-Piccard-Hof 1, 8093 Zurich, Switzerland

[7] RIKEN Center for Integrative Medical Sciences, 1-7-22 Suehiro-cho Tsurumi-ku, Yokohama City, Kanagawa 230-0045, Japan

[8] Center for Microscopy and Image Analysis, University of Zurich, Winterthurerstrasse 190, 8057 Zurich, Switzerland

[9] Department of Microbial and Cellular Sciences, Faculty of Health and Medical Sciences, University of Surrey, Stag Hill Campus 19 AX 01, GU2 7XH Guildford, UK

[10] Faculty of Science, University of Zurich, Winterthurerstrasse 190, 8057 Zurich, Switzerland

[11] Present address: Department of Biochemistry, University of Zurich, Winterthurerstrasse 190, 8057 Zurich, Switzerland

[12] Present address: University Children's Hospital Basel, University of Basel, Spitalstrasse 33, 4056 Basel, Switzerland

[13] Present address: Department of Pathology, NYU School of Medicine, New York, NY 10016, USA

[14] Present address: Laura & Isaac Perlmutter Cancer Center, NYU School of Medicine, New York, NY 10016, USA